Supplementary Material

Tailoring d-band Center of Porous CoS_2 Nanospheres via Low-Electronegative Fe for Weakened OH* Adsorption and Boosted Oxygen Evolution

Heyuan Chen[a], Wei Wu[a], Suhao Chen[a], Zichen Wang[a], Runzhe Chen[a], Niancai Cheng*[a,b]

[a] *College of Materials Science and Engineering, Fuzhou University, Fuzhou 350108, Fujian, China. E-mail address: niancaicheng@fzu.edu.cn.*

[b] Key Laboratory of Advanced Energy Materials Chemistry (Ministry of Education), Nankai University, Tianjin 300071, China

* *Corresponding author. E-mail address: niancaicheng@fzu.edu.cn (N. C. Cheng).*

Experimental section

Reagents. All the chemicals used were commercial without any further purification. Zinc nitrate hexahydrate ($Zn(NO_3)_2 \cdot 6H_2O$; >99.0%, Sinopharm Chemical Reagent Co., Ltd.), Ferric nitrate nonahydrate ($Fe(NO_3)_3 \cdot 9H_2O$; >99.0%, Sinopharm Chemical Reagent Co., Ltd.), Cobalt nitrate hexahydrate ($Co(NO_3)_2 \cdot 6H_2O$; >99.0%, Sinopharm Chemical Reagent Co., Ltd.), 2-methyleimidazole (99.0%, Aladdin), sulfur powder(99.9%, Sinopharm Chemical Reagent Co., Ltd.), potassium hydroxide (KOH; 85%, Sinopharm Chemical Reagent Co., Ltd.) and de-ionized water with the specific resistance of 18.25 $M\Omega \cdot cm^{-1}$ (obtained by reversed osmosis followed by ion-exchange and filtration).

Characterizations

Characterization: Scanning electron microscopy (SEM) was performed on a SUPRA 55. Transmission electron microscopy (TEM) images and Wide-angle X-ray diffraction (XRD, D-MAX 2200 VPC) patterns. X-ray photoelectron spectroscopy (XPS) characterization was performed by an K-Alpha. The nitrogen absorption-desorption isotherms were measured using the equipment of Micromeritics 3Flex. Raman spectra was performed

by DXR2Xi. The total specific surface area was calculated from the Brunauer-Emmett-Teller (BET) equation. The pore size distribution (PSD) curves were calculated by the nonlocal density functional theory (DFT).
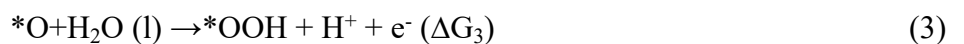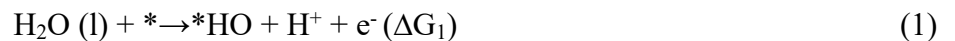
Electrochemical Measurements. The electrochemical tests were measured with a three-electrode system on an electrochemical workstation (CHI660E). A glassy carbon electrode (diameter of 5 mm with surface area of 0.196 cm^{-2}) was used as a working electrode, while a carbon rod was utilized as the counter electrode. Hg/HgO electrode was used as the reference electrode. In respect of preparing working electrode, 4 mg catalysts mixed with 20 μL Nafion solution (Sigma Aldrich, 5 wt%) were dispersed in 800 μL of water–isopropanol solution with volume ratio of 1:1 by sonicating for at least 10 min to form a homogeneous ink. The catalyst ink was then drop-casted onto the glassy carbon electrode with a 0.38 mg cm-2 loading for all samples. Oxygen was used to purge the 1 M KOH solution for 30 min to keep the solution oxygen saturation before OER catalytic activity testing. Before LSV tests, the working electrodes were stabilized by CV test at a scan rate of 100 mV s^{-1} from 1.2 to 1.6 V (vs RHE) for 30 cycles. The LSV polarization curves of OER process were conducted at a rate of 5 mV s^{-1} with ohmic potential drop (iR) correction. The electrochemical impedance spectroscopy (EIS) measurements are carried out in the frequency range from 10 kHz to 0.1 Hz. The electrode durability was tested by repetitive CV scan for 1000 cycles in a potential window of 1.2 to 1.6 V (vs RHE) and Chronopotentiometry measurement of 10 mA cm^{-2} for 10000 s. The C_{dl} was calculated by performing CV measurements at different scan rates of 20, 40, 60, 80 and 100 mV s^{-1} in the potential range of 1.00–1.10 V (vs RHE). The value of C_{dl} was a half of the linear slope obtained from plotting $\Delta j = j_a\text{-}j_c$ at 1.05 V against the scan rates (j_a and j_c are anode and cathode current density, respectively). The TOF value was calculated by the following equation: TOF = $j\cdot S/\alpha\cdot F\cdot n$, where j is the current density (mA cm^{-2}) at $\eta = 310$ mV, S represents the surface area of as-prepared electrode, the α means the electron number of the target product (electrons/mol), F is the Faraday's constant (96485.3 C mol^{-1}), and n represents the moles of Co atoms on the electrode which can be calculated by the loading weight and the molecular weight of the coated catalysts. The Faraday efficiency (FE) was calculated by

the following equation: FE = V_{exp}/V_{theo} where V_{exp} and V_{theo} are the volume of the generated O_2 gas (mL) and

the calculated volume of O_2 (mL), respectively. The latter was calculated based on the equation of $V_{theo.}$

$=V_MQ/nF$, where V_M is the molar volume of the ideal gas (24.5 L mol^{-1}), Q is electric charge quantity (C), n is

electron transferred number (n = 4 for OER), and F is the Faraday constant (96,485 C mol^{-1}). All the potentials

were calibrated to the reversible hydrogen electrode (vs RHE), and the corresponding equation is $E_{RHE} = E_{Hg/HgO}$

+0.098+ 0.059pH.

Density functional theory (DFT) calculations.

Density functional theory (DFT) calculations were used to optimize the lattice constants and ionic positions of

the pristine CoOOH, $Fe_{0.25}Co_{0.75}OOH$, $Fe_{050}Co_{0.50}OOH$, $Fe_{0.75}Co_{0.25}OOH$ and FeOOH structure. It is reasonable

to choose the kinetic energy cutoff for plane wave expansion at 450 eV and a 3×3×1 Monkhorst-Pack k-point

grid sampling of the first Brillouin zone. In order to determine the occupancy, we set the Gaussian smearing

width to 0.1 eV. The adsorption surface, of which the unit lattice constant is set to 12.215 Å×12.215 Å and the

vacuum layer is set to 30 Å, was calculated the structural relaxation by using a conjugate gradient algorithm,

limiting the maximum force and energy of unconstrained atoms to less than 0.01 eV/Å and 1×10-6 eV, 6

respectively. The electronic iteration convergence value for self-consistent field (SCF) calculation was set to

1×10-6 eV.

The thermodynamic model of water oxidation proposed by Norskov and coworkers , which is composed

of four electrochemical steps, each of which constitutes one proton transfer, was used in this work. The following

electron reaction paths are considered for the oxygen evolution reaction (OER) process:

$$H_2O \text{ (l)} + * \rightarrow *HO + H^+ + e^- (\Delta G_1) \tag{1}$$

$$*HO \rightarrow *O + H^+ + e^- (\Delta G_2) \tag{2}$$

$$*O + H_2O \text{ (l)} \rightarrow *OOH + H^+ + e^- (\Delta G_3) \tag{3}$$

$$*OOH \rightarrow O_2 \text{ (g)} + * + H^+ + e^- (\Delta G_4) \tag{4}$$

The adsorption energies (ΔE_{ads}) of OOH*, OH* and O* are calculated by referring their DFT total energy, and H_2O and H_2 in the gas phase. The adsorption free energy (ΔG_{ads}) is obtained by

$$\Delta G_{ads} = \Delta E_{ads} + \Delta ZPE - T\Delta S \qquad (5)$$

where ΔZPE and ΔS are the contributions to the free energy from the zero-point vibration energy and entropy, respectively. For each reaction step in OER, the Gibbs free energy of formation is given by

$$\Delta G = \Delta E_{DFT} + \Delta ZPE - T\Delta S - eU \qquad (6)$$

where ΔE_{DFT}, ΔZPE and ΔS are the change of DFT total energy, zero-point energy, and entropy from the initial to the final state; U is the electrode potential and e is the charge transferred. The reference potential is set to be that of the standard hydrogen electrode.
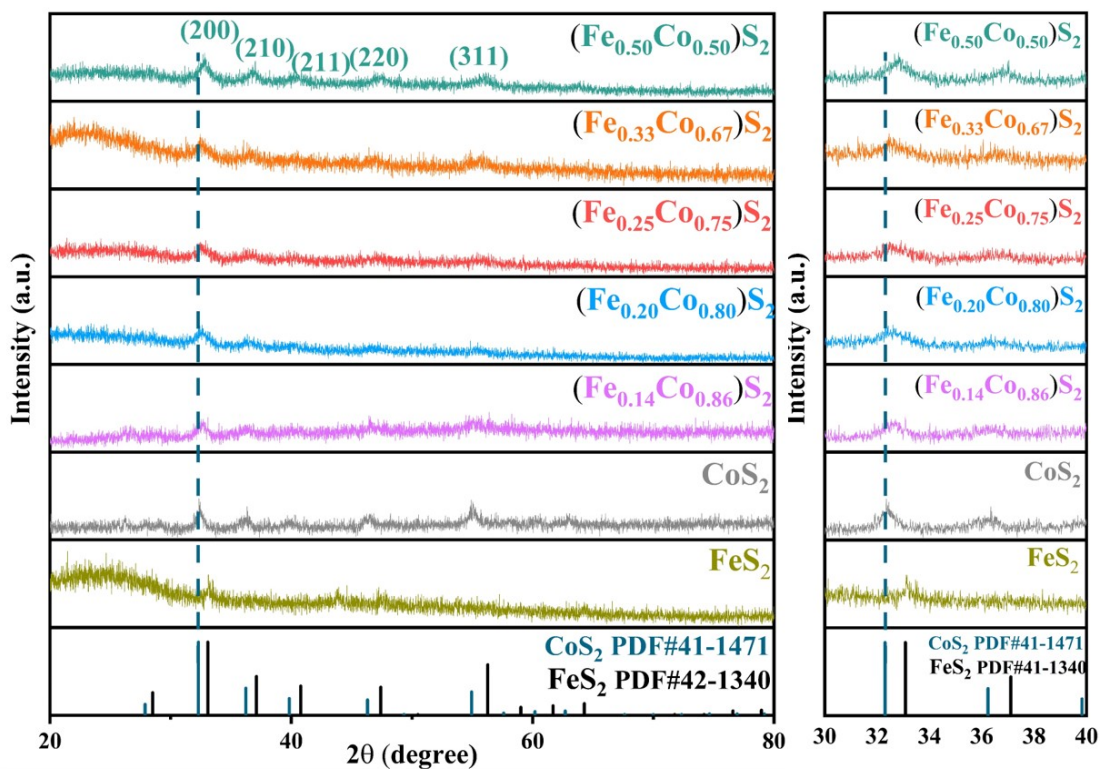
Fig. S1 XRD patterns of CoS_2, $(Fe_{0.50}Co_{0.50})S_2$, $(Fe_{0.33}Co_{0.37})S_2$, $(Fe_{0.25}Co_{0.75})S_2$, $(Fe_{0.20}Co_{0.80})S_2$, $(Fe_{0.14}Co_{0.86})S_2$ and FeS_2.
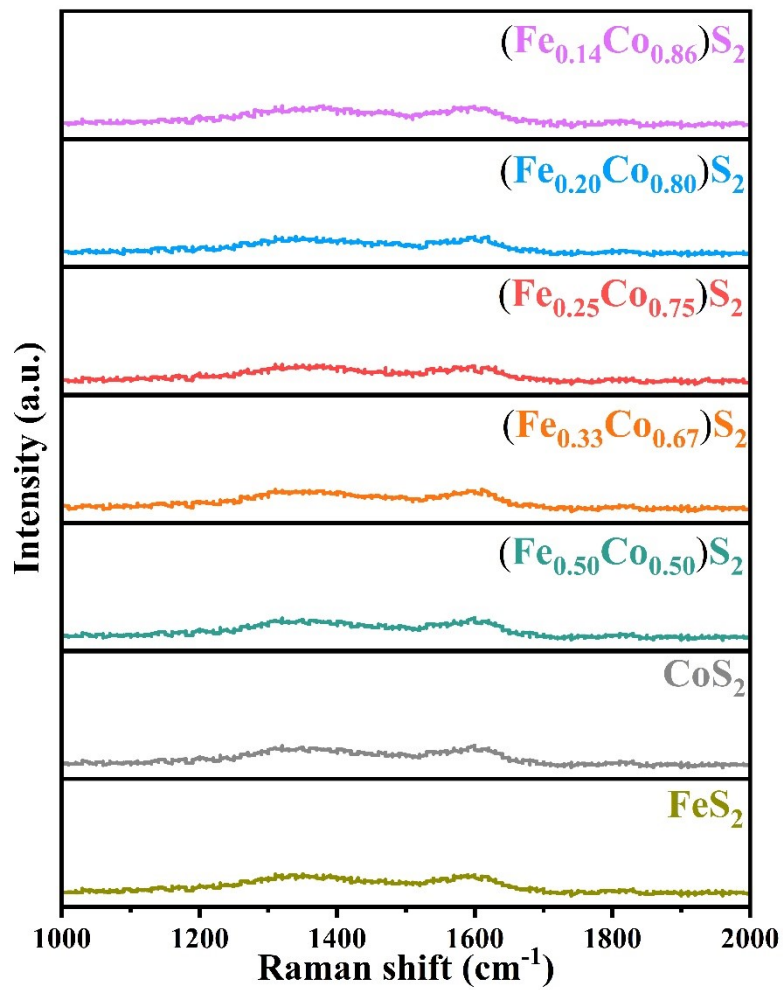
Fig. S2 Raman spectra of $(Fe_xCo_{1-x})S_2$.
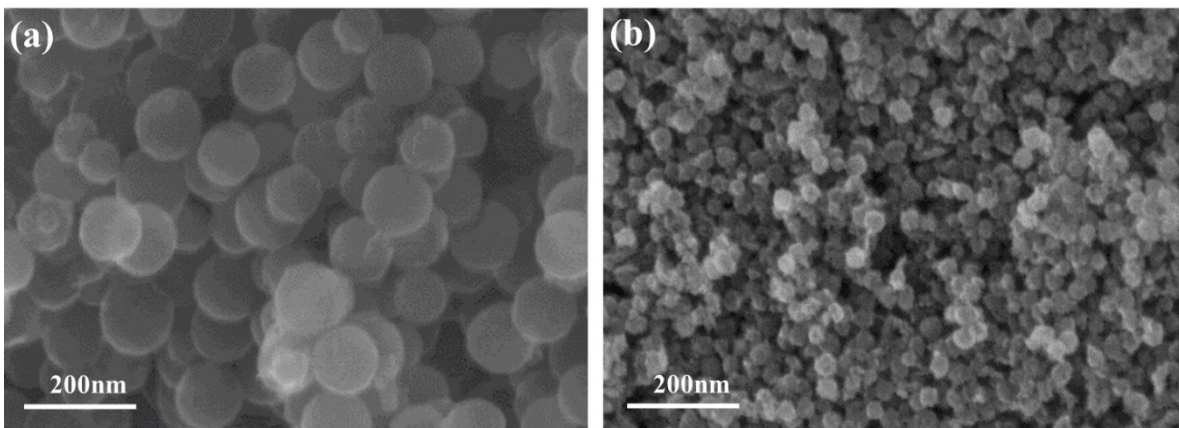
Fig. S3 SEM images of (a, b) spherical ZIF-8 and Fe-Co$_3$O$_4$.
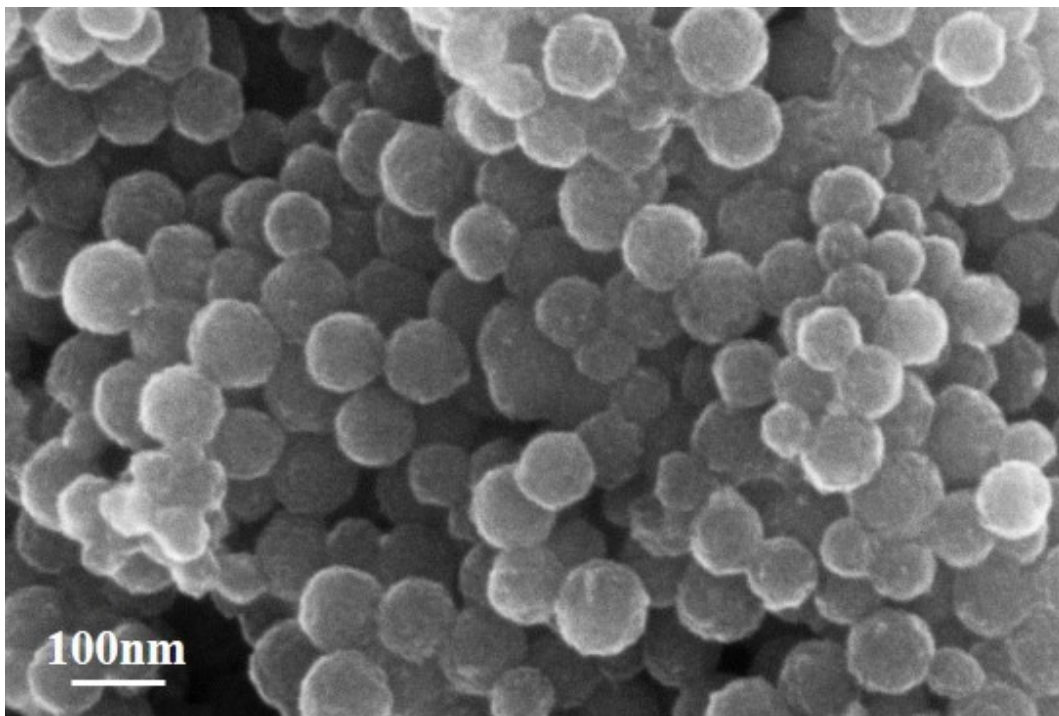
Fig. S4 SEM images of CoS_2.
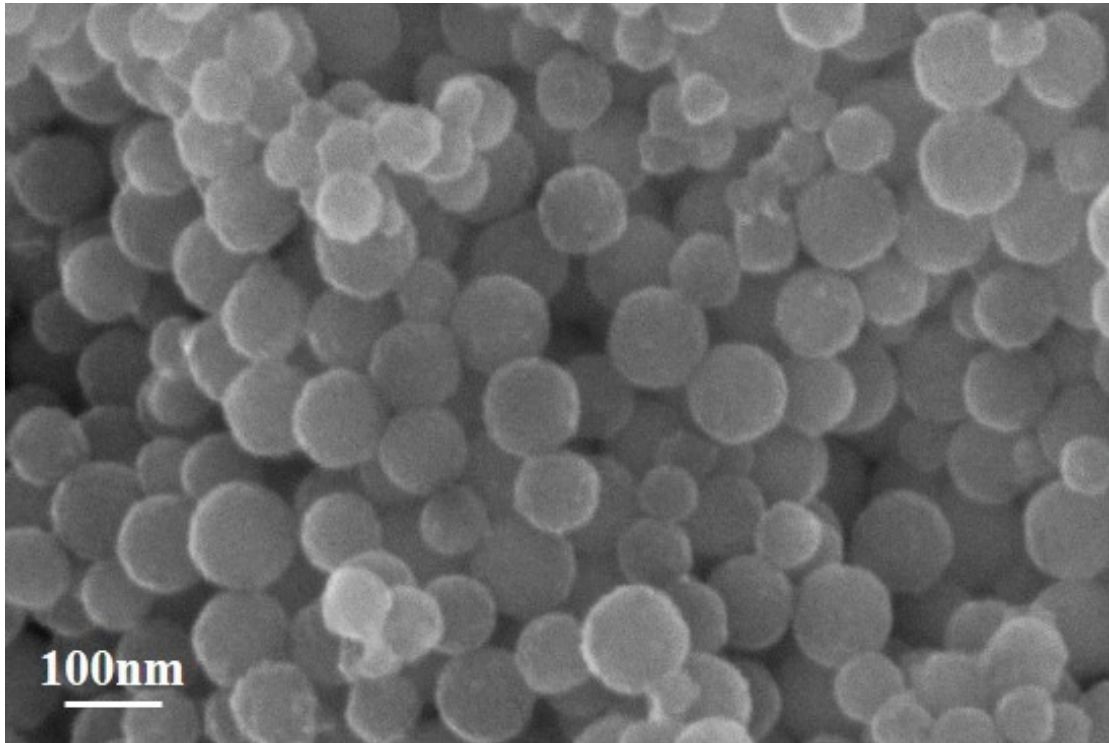
Fig. S5 SEM images of $(Fe_{0.50}Co_{0.50})S_2$.
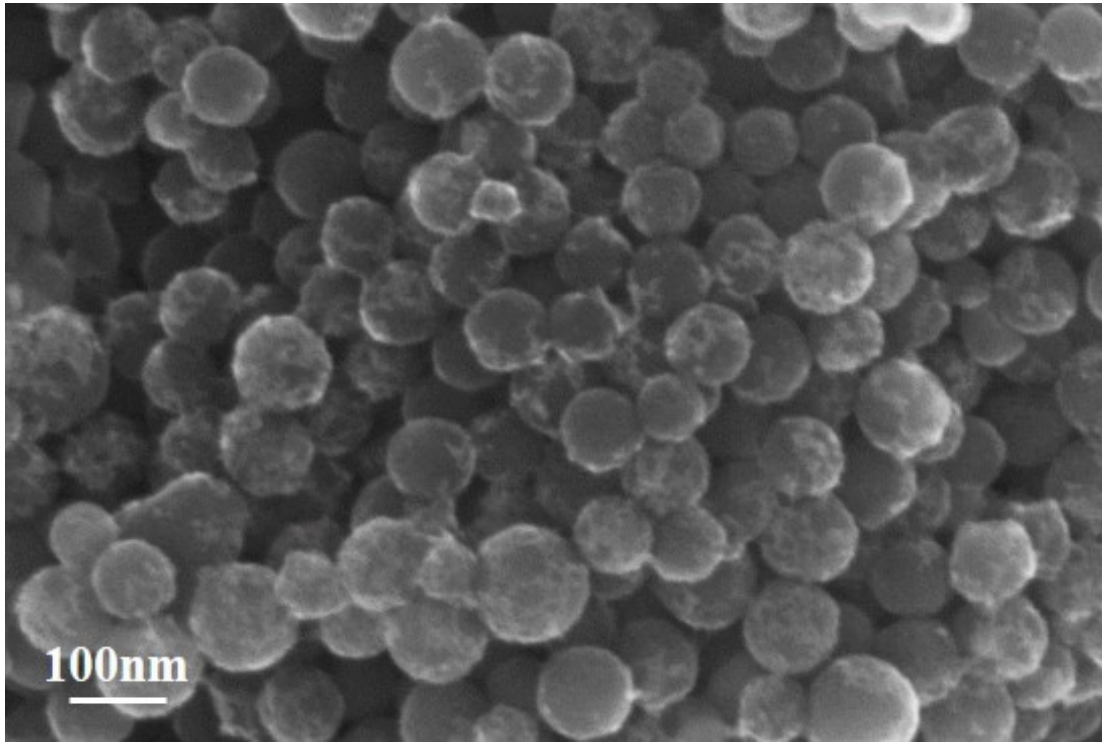
Fig. S6 SEM images of $(Fe_{0.33}Co_{0.67})S_2$.
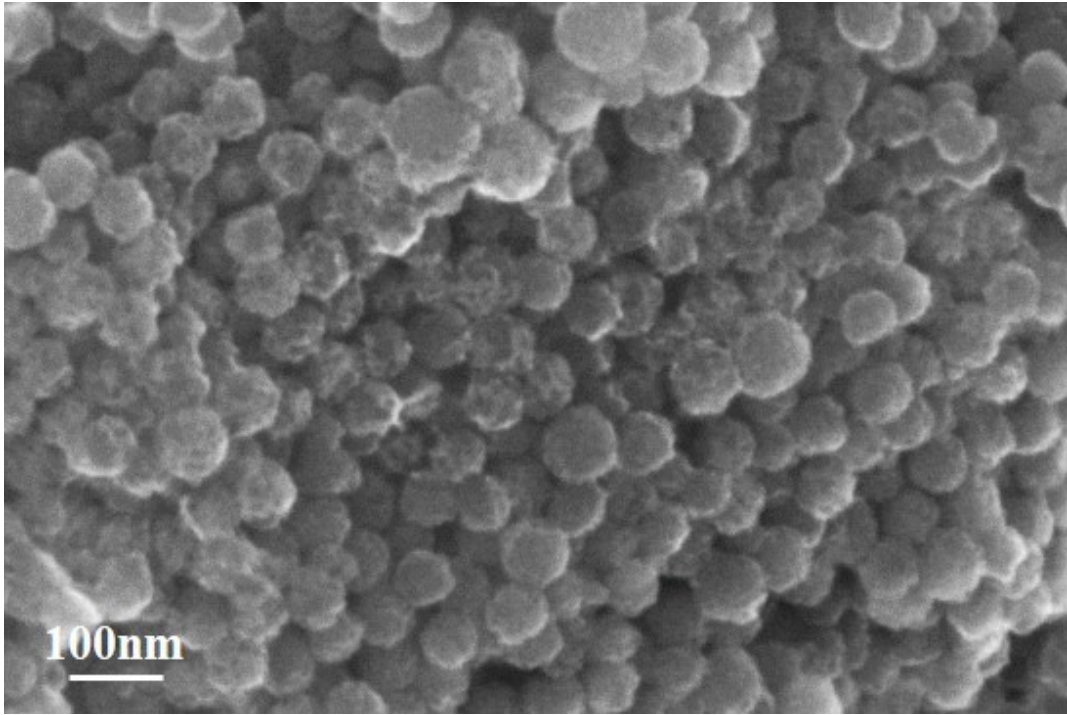
Fig. S7 SEM images of $(Fe_{0.25}Co_{0.75})S_2$.
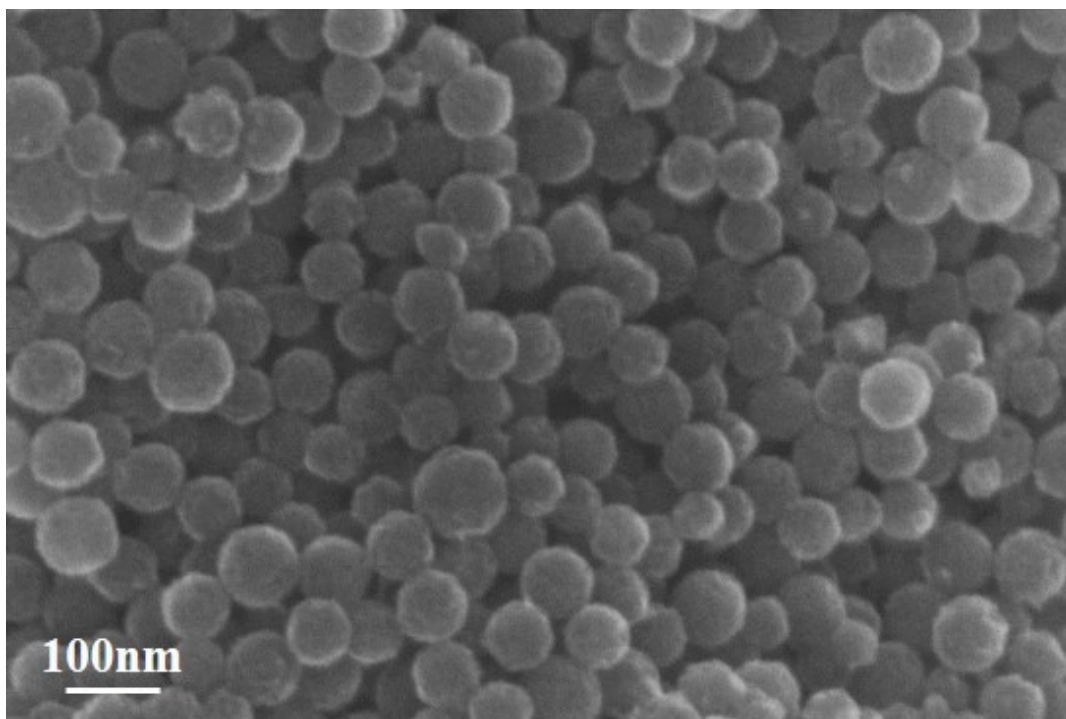
Fig. S8 SEM images of $(Fe_{0.20}Co_{0.80})S_2$.
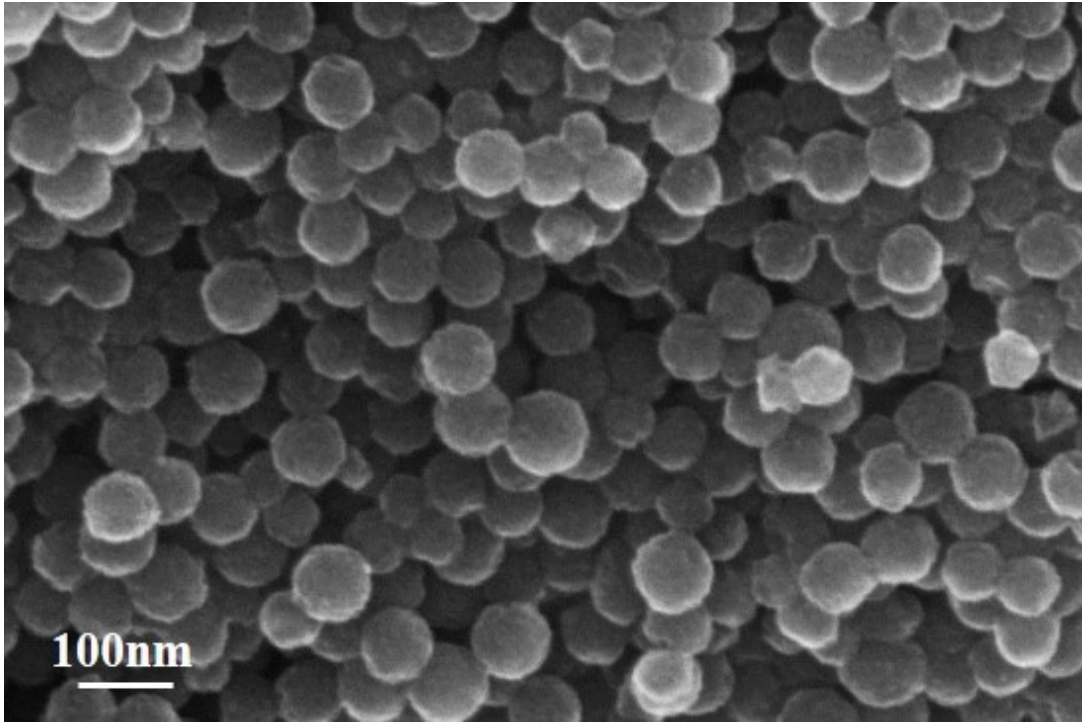
Fig. S9 SEM images of $(Fe_{0.16}Co_{0.84})S_2$.
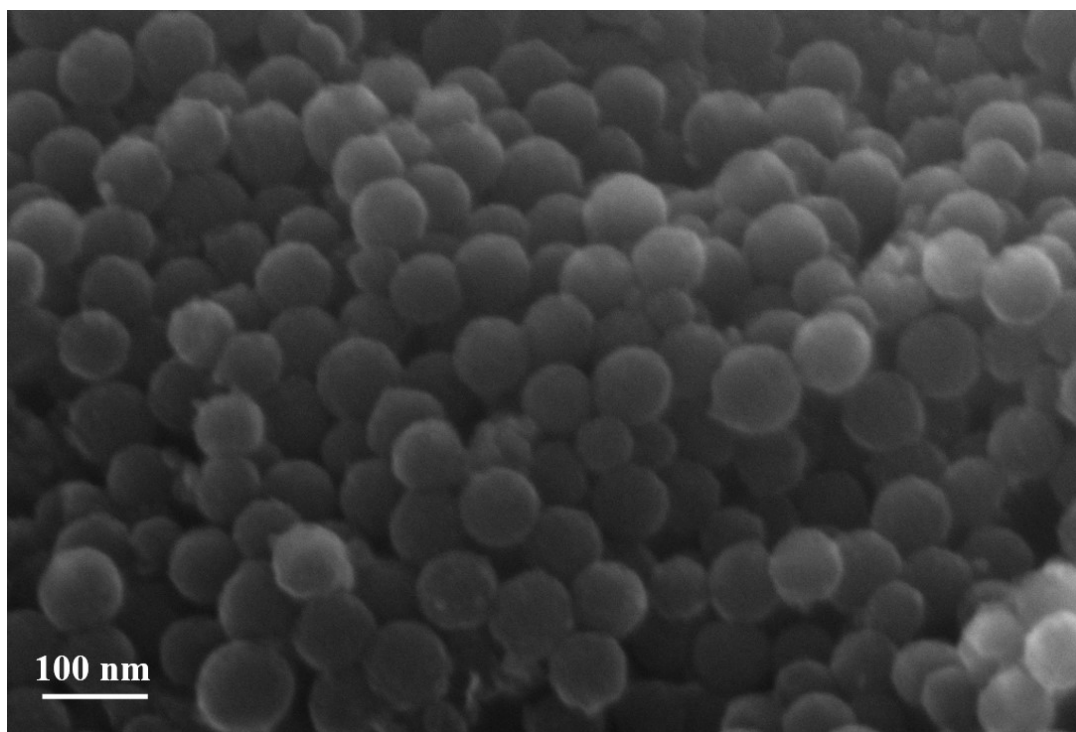
Fig. S10 SEM images of FeS$_2$.
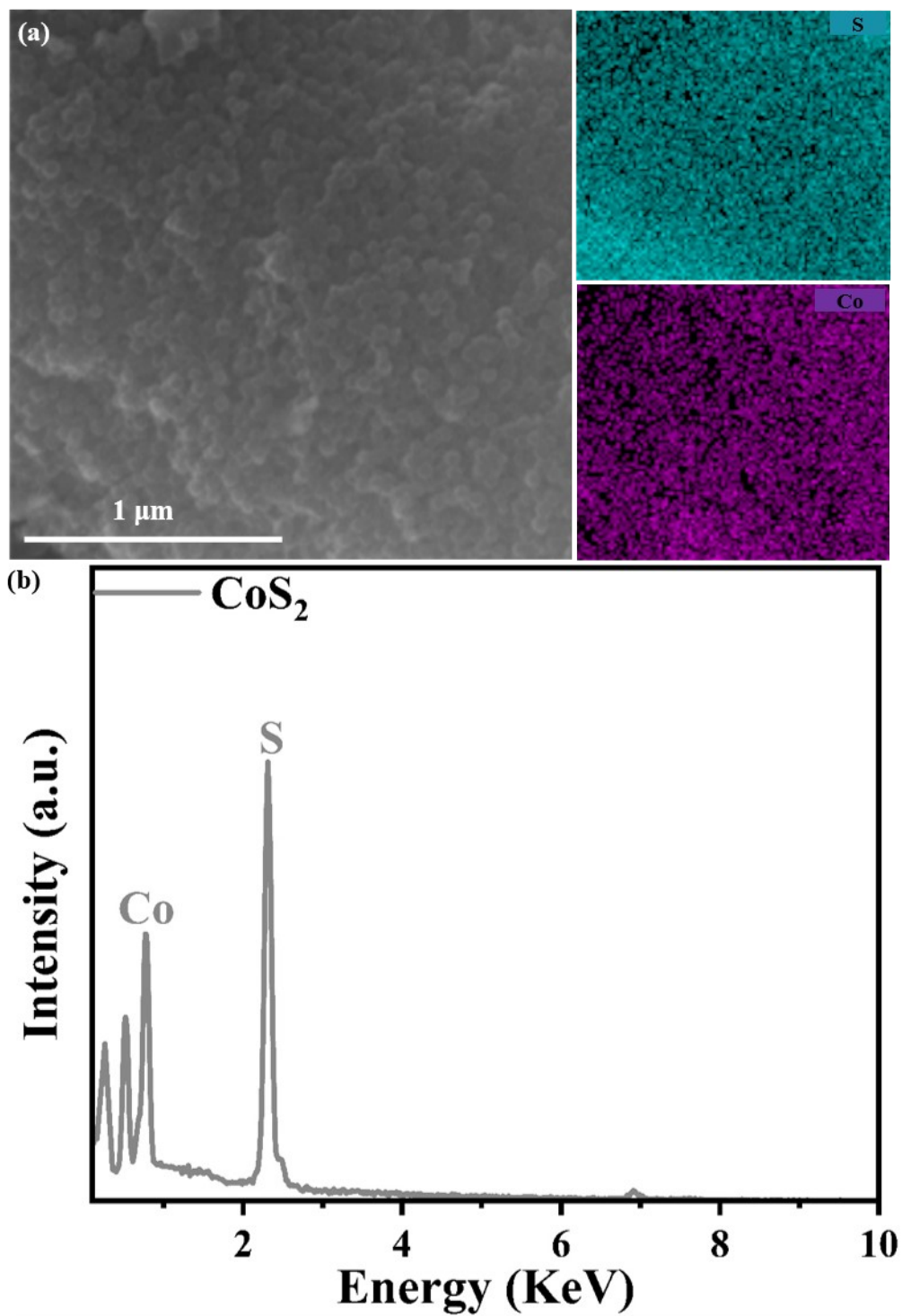
Fig. S11 (a) SEM image and corresponding EDS element mapping images of CoS_2. (b) SEM-EDS spectrum of CoS_2.
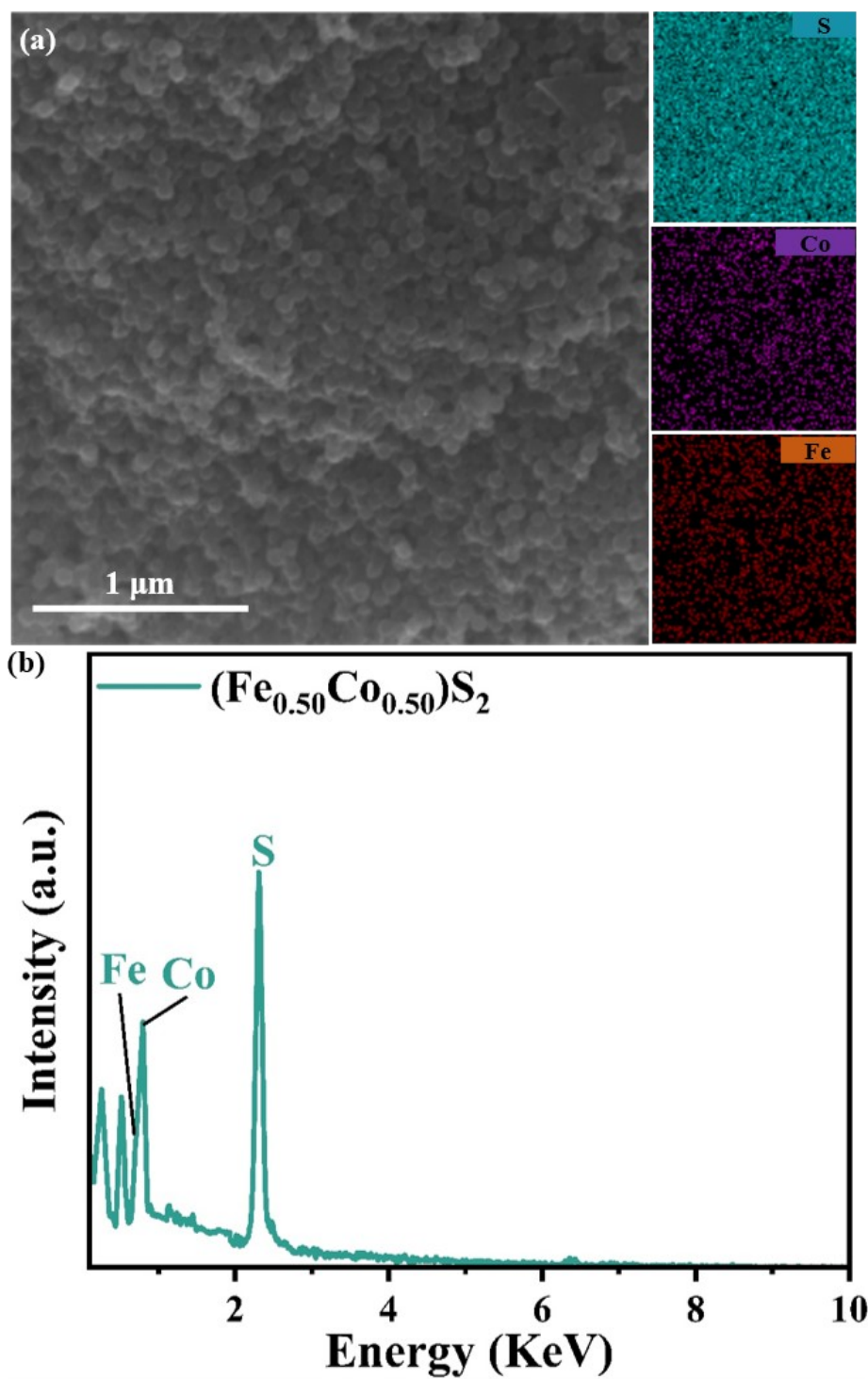
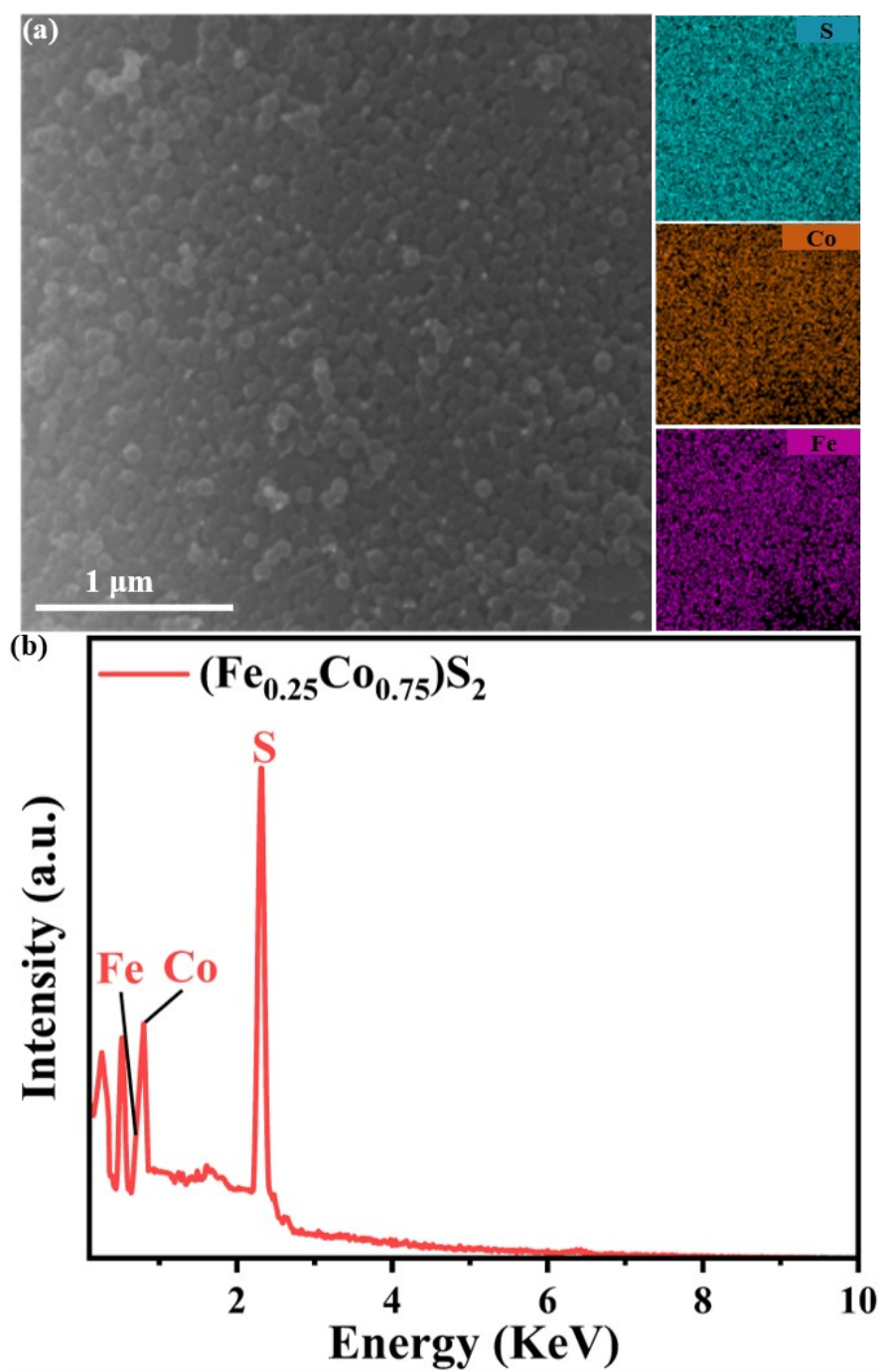**Fig. S12** (a) SEM image and corresponding EDS element mapping images of$(Fe_{0.50}Co_{0.50})S_2$. (b) SEM-EDS

spectrum of $(Fe_{0.50}Co_{0.50})S_2$.
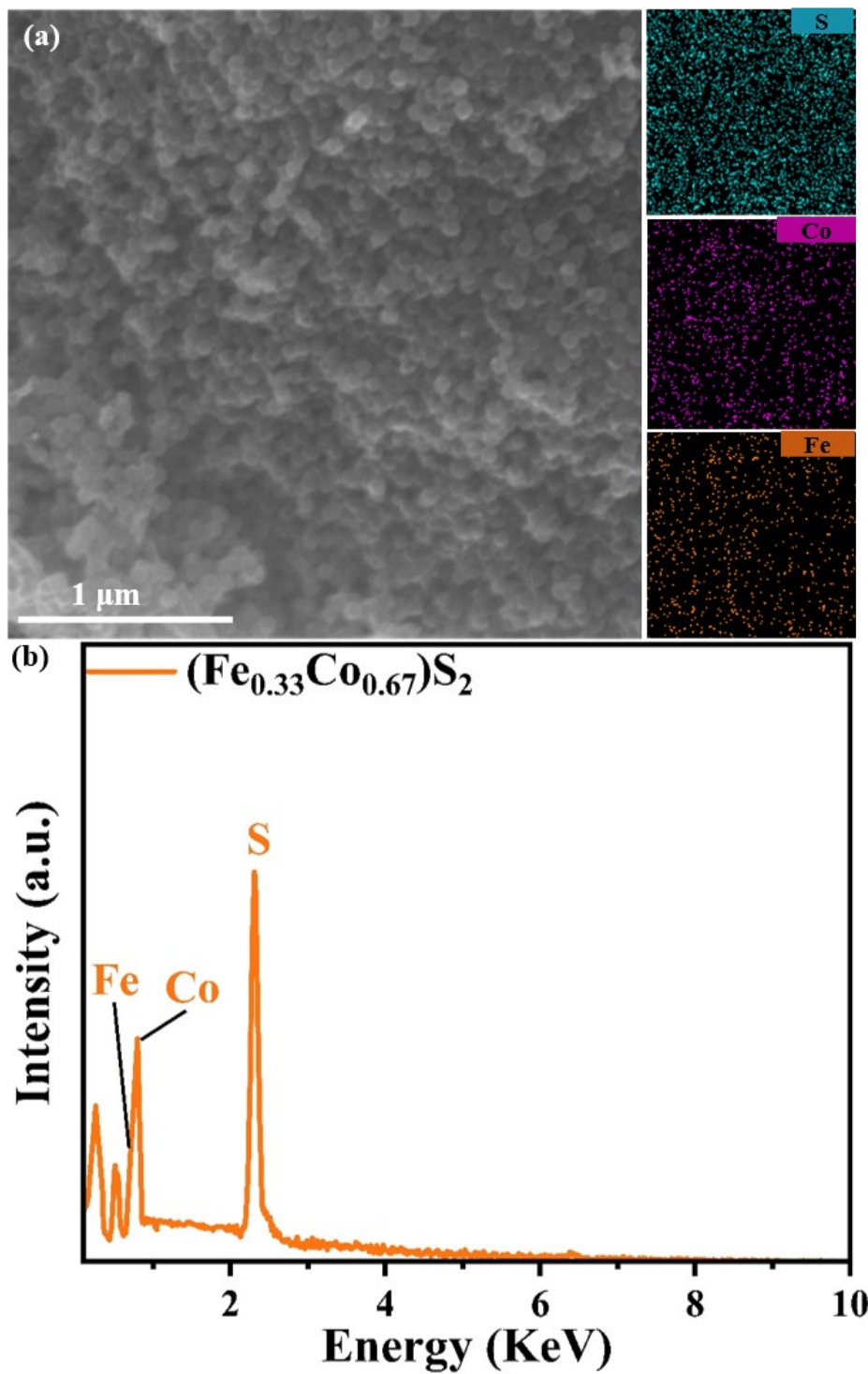
Fig. S13 (a) SEM image and corresponding EDS element mapping images of $(Fe_{033}Co_{0.67})S_2$. (b) SEM-EDS

spectrum of $(Fe_{0.33}Co_{0.67})S_2$.

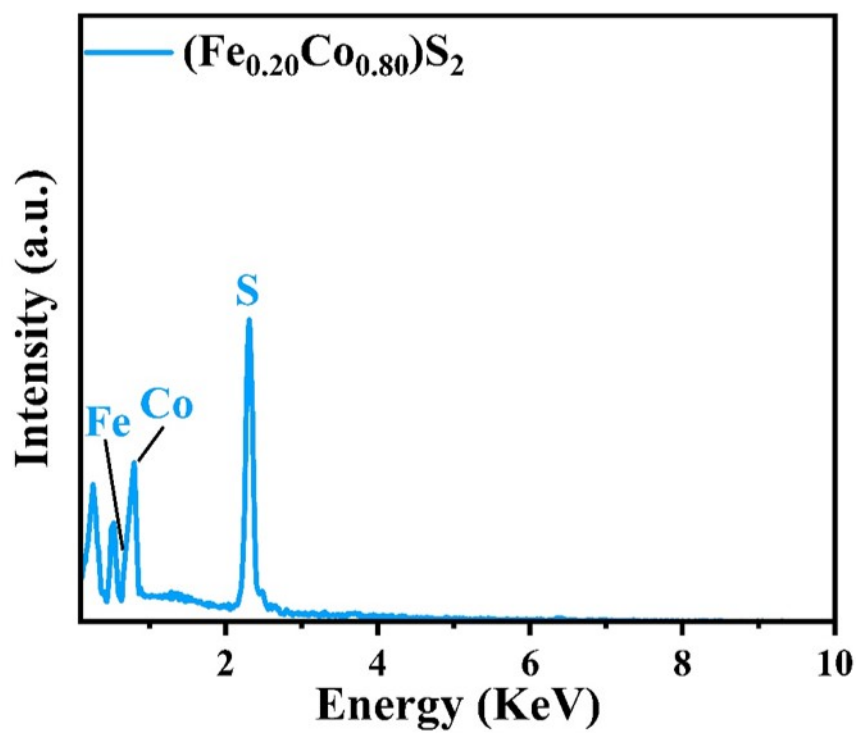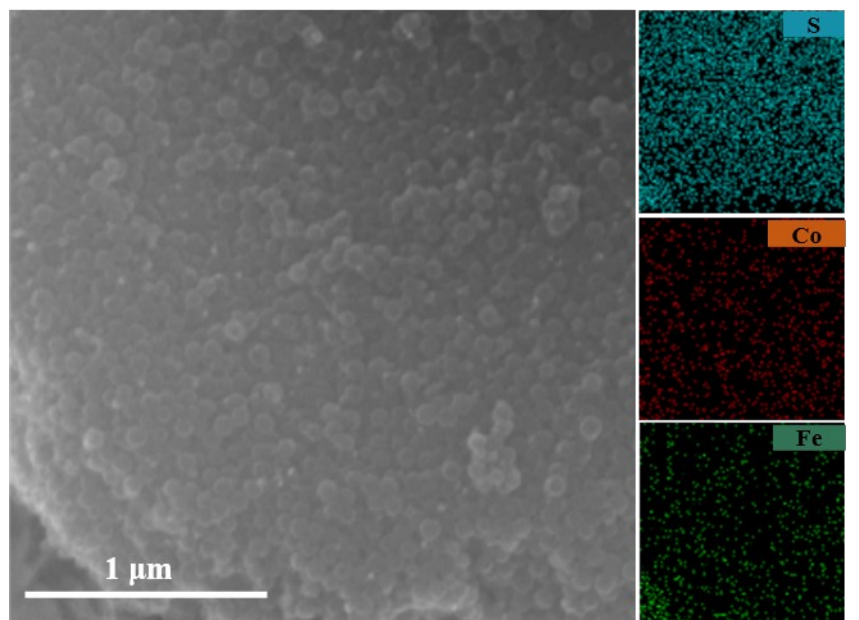**Fig. S14** (a) SEM image and corresponding EDS element mapping images of $(Fe_{0.25}Co_{0.75})S_2$. (b) SEM-EDS spectrum of $(Fe_{0.25}Co_{0.75})S_2$.

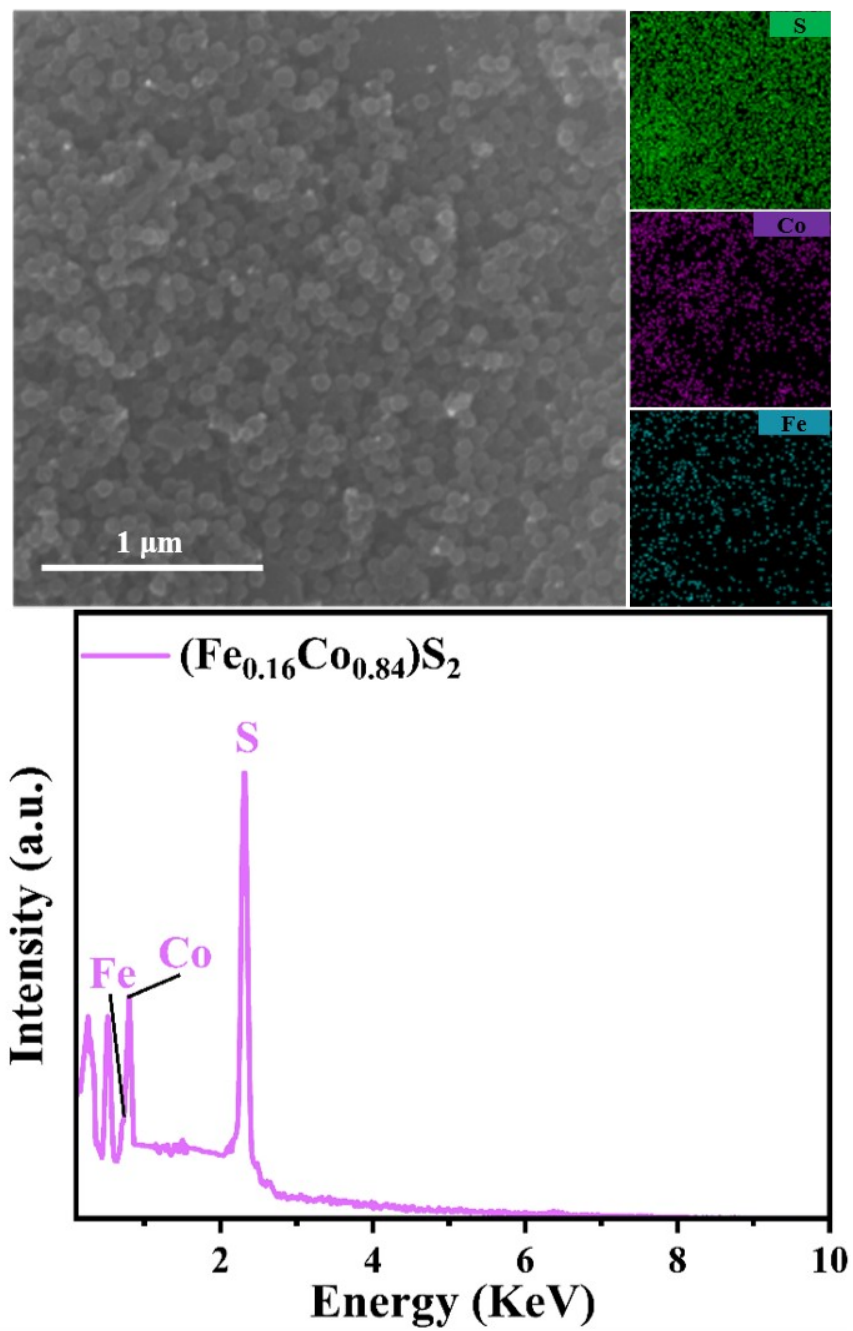**Fig. S15** (a) SEM image and corresponding EDS element mapping images of$(Fe_{0.20}Co_{0.80})S_2$. (b) SEM-EDS spectrum of $(Fe_{0.20}Co_{0.80})S_2$.

Fig. S16 (a) SEM image and corresponding EDS element mapping images of $(Fe_{0.16}Co_{0.84})S_2$. (b) SEM-EDS spectrum of $(Fe_{0.16}Co_{0.84})S_2$.
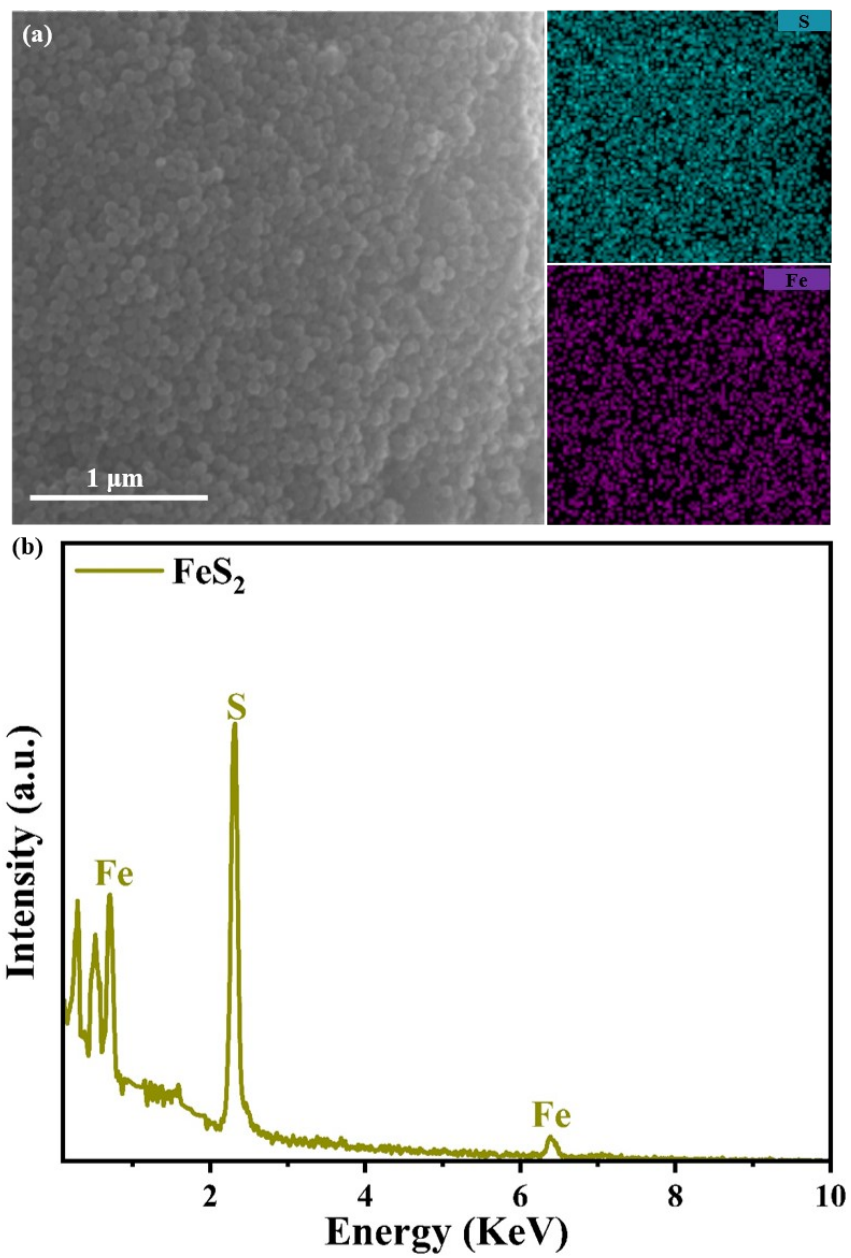
Fig. S17 (a) SEM image and corresponding EDS element mapping images of FeS_2. (b) SEM-EDS spectrum of FeS_2.
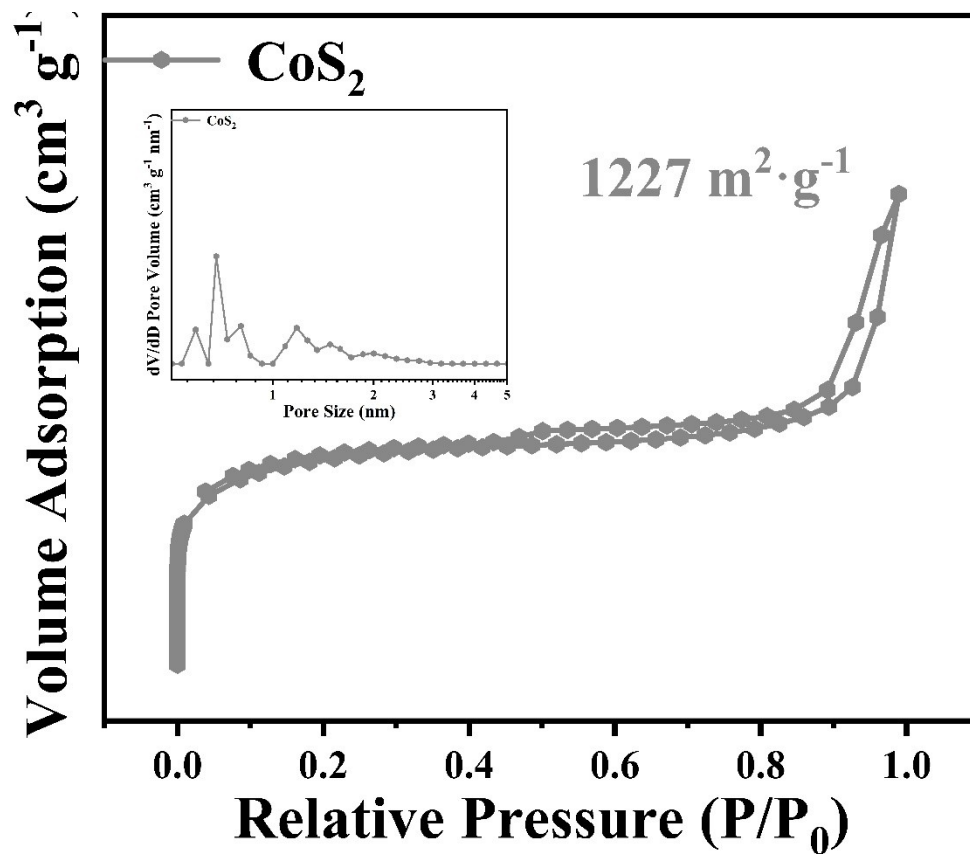
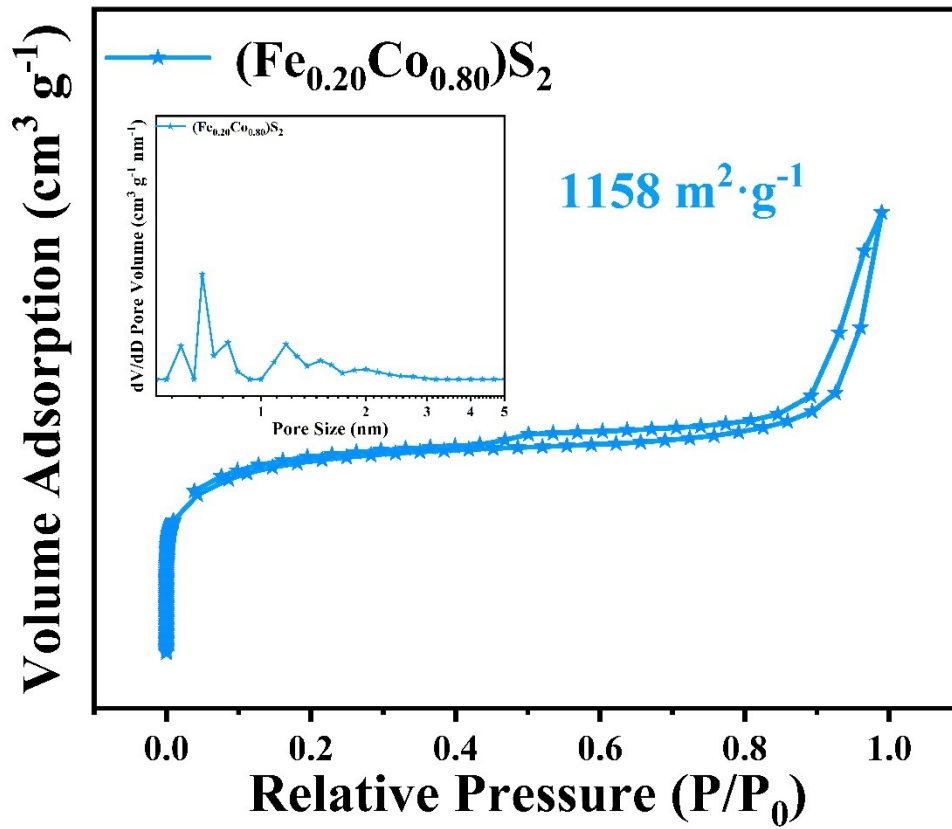**Fig. S18** N_2 adsorption−desorption isotherms and pore size distribution of CoS_2.

Fig. S19 N$_2$ adsorption−desorption isotherms and pore size distribution of (Fe$_{0.20}$Co$_{0.80}$)S$_2$.

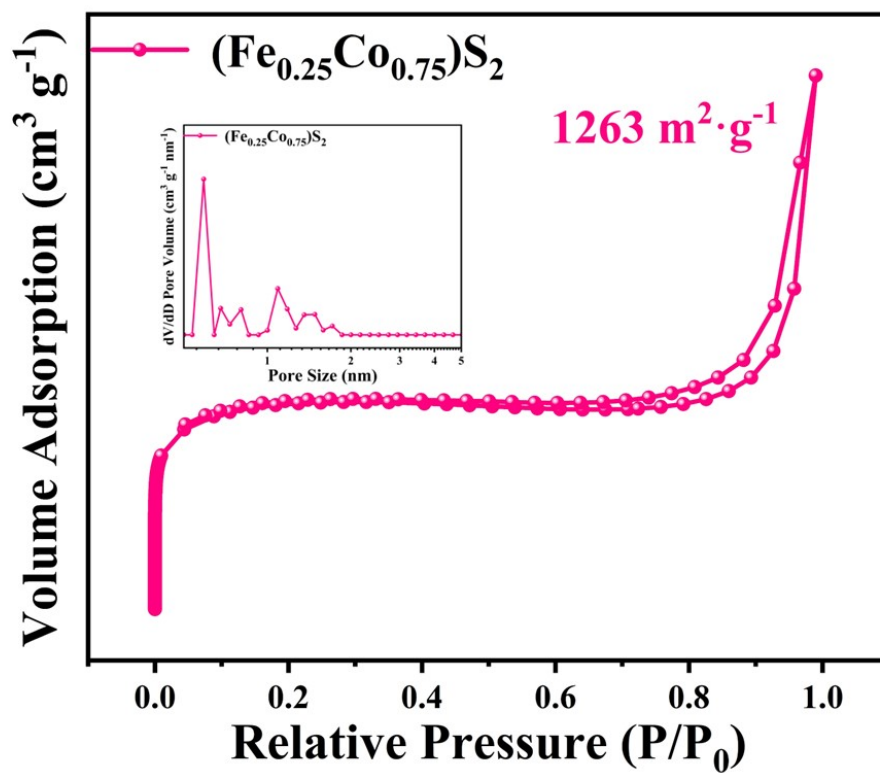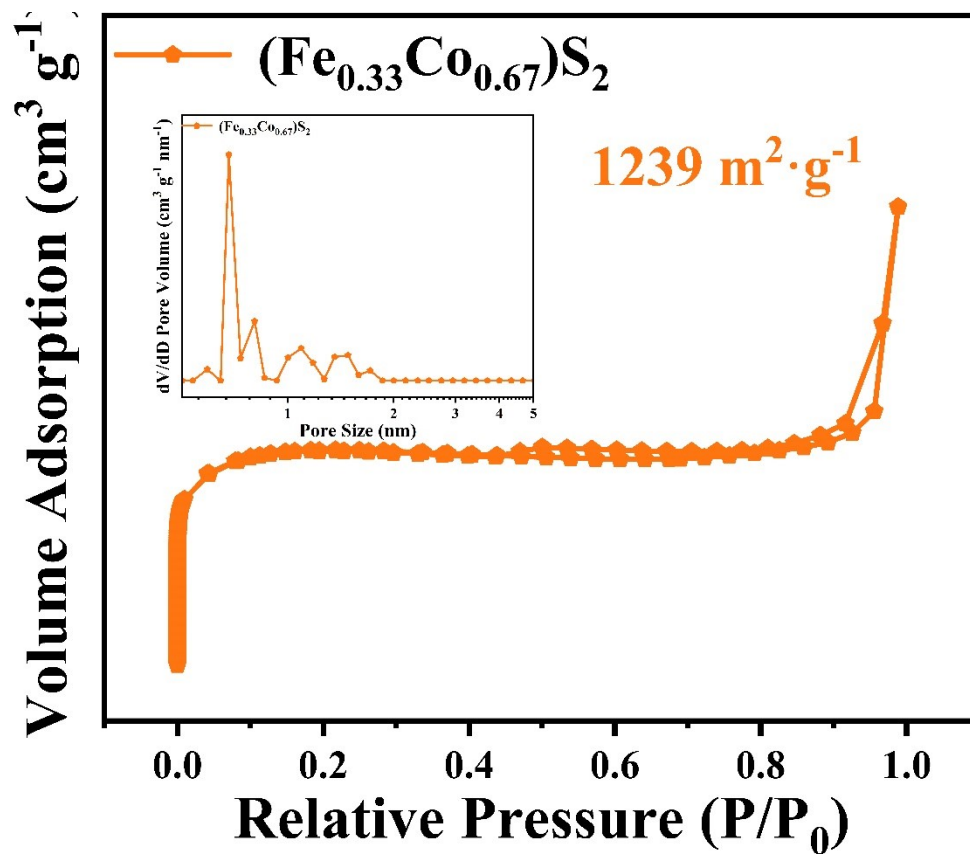**Fig. S20** N_2 adsorption−desorption isotherms and pore size distribution of $(Fe_{0.25}Co_{0.75})S_2$.

Fig. S21 N$_2$ adsorption−desorption isotherms and pore size distribution of (Fe$_{0.33}$Co$_{0.67}$)S$_2$.
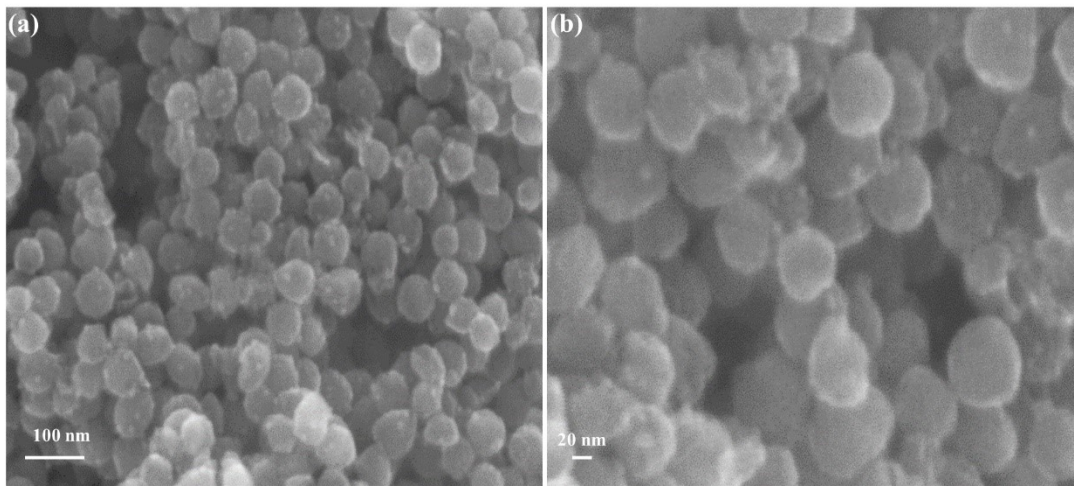
Fig. S22 (a-b) SEM images of $(Fe_{0.25}Co_{0.75})S_2$-S.
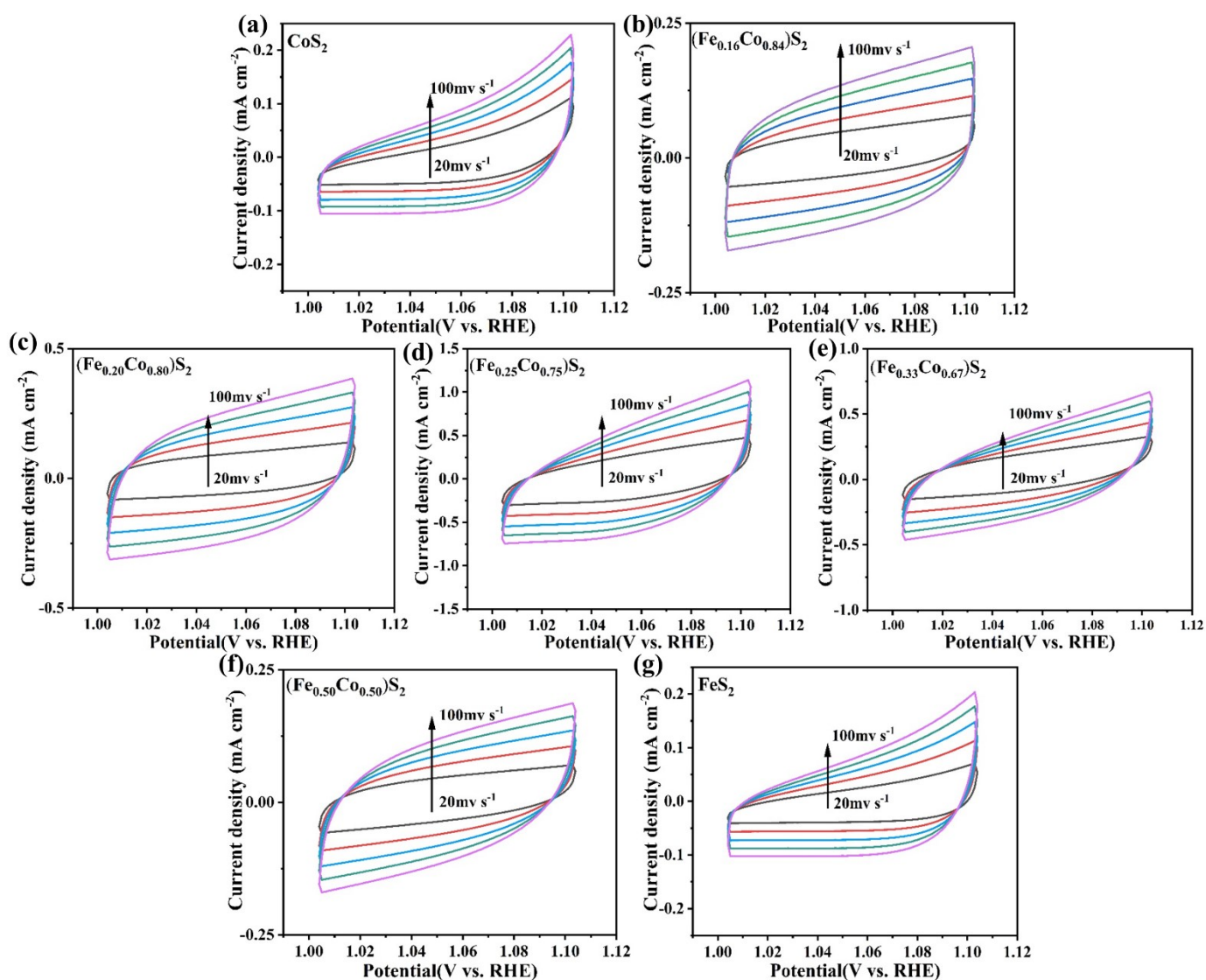
Fig. S23 Cyclic voltammograms curves of (a-g) CoS_2, $(Fe_{0.50}Co_{0.50})S_2$, $(Fe_{0.33}Co_{0.67})S_2$, $(Fe_{0.25}Co_{0.75})S_2$, $(Fe_{0.20}Co_{0.80})S_2$, $(Fe_{0.16}Co_{0.84})S_2$ and FeS_2 with the scan rates of 20, 40, 60, 80, and 100 mV S^{-1}.
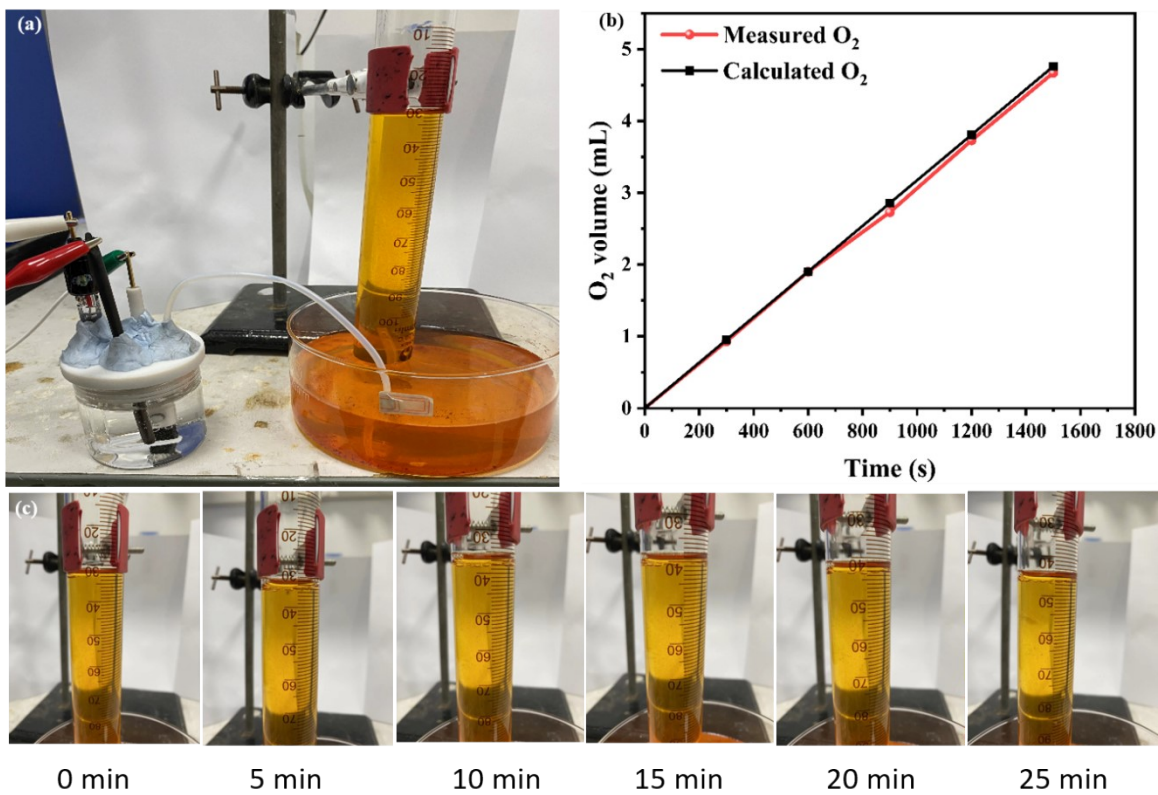
Fig. S24 (a) Faraday efficiency test system. (b)Measured O_2 generation at 50 mA cm^{-2} and the associated FE. (c) Oxygen generation at different test times.
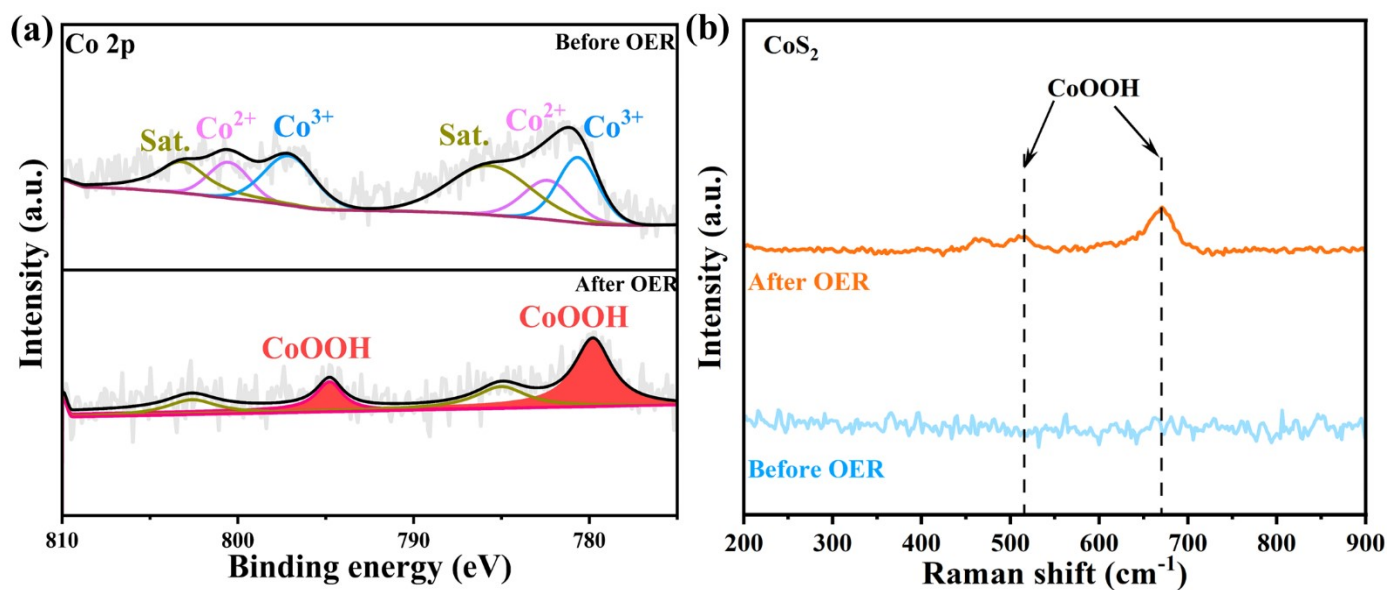
Fig. S25 (a) XPS spectra of Co 2p for CoS_2 electrocatalyst before and after the OER reaction. (b) Raman spectra of CoS_2 before and after a 10 000 s OER stability test.
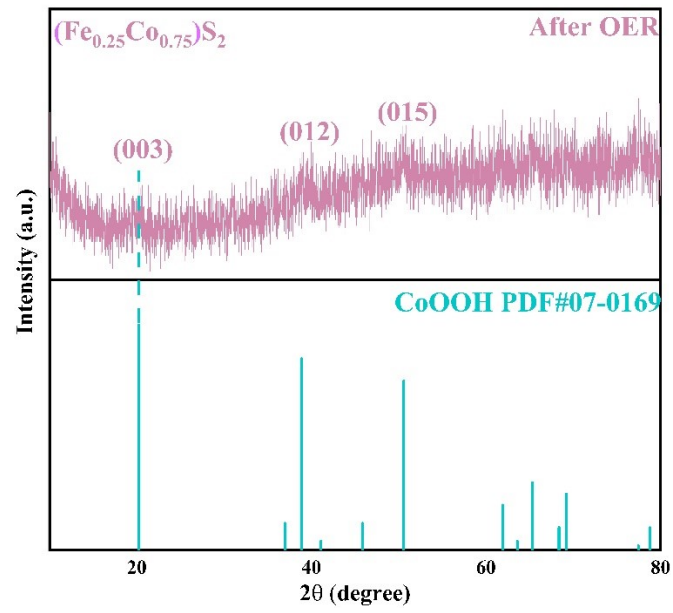
Fig. S26 XRD pattern of $(Fe_{0.25}Co_{0.75})S_2$ after OER test.
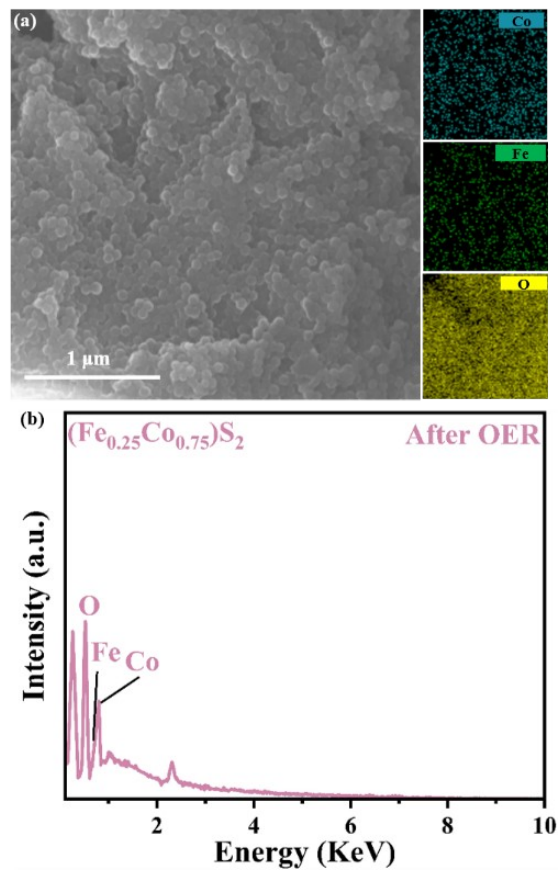
Fig. S27 (a) SEM image and corresponding EDS element mapping images of $(Fe_{0.25}Co_{0.75})S_2$ after OER test. (b) SEM-EDS spectrum of $(Fe_{0.25}Co_{0.75})S_2$ after OER test.
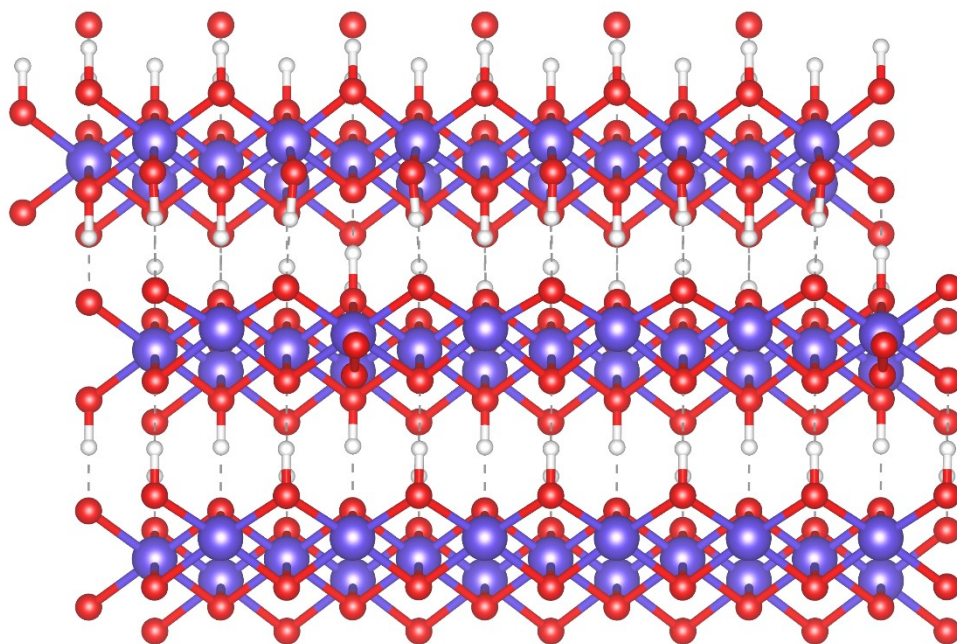
Fig. S28 Model structure of CoOOH.
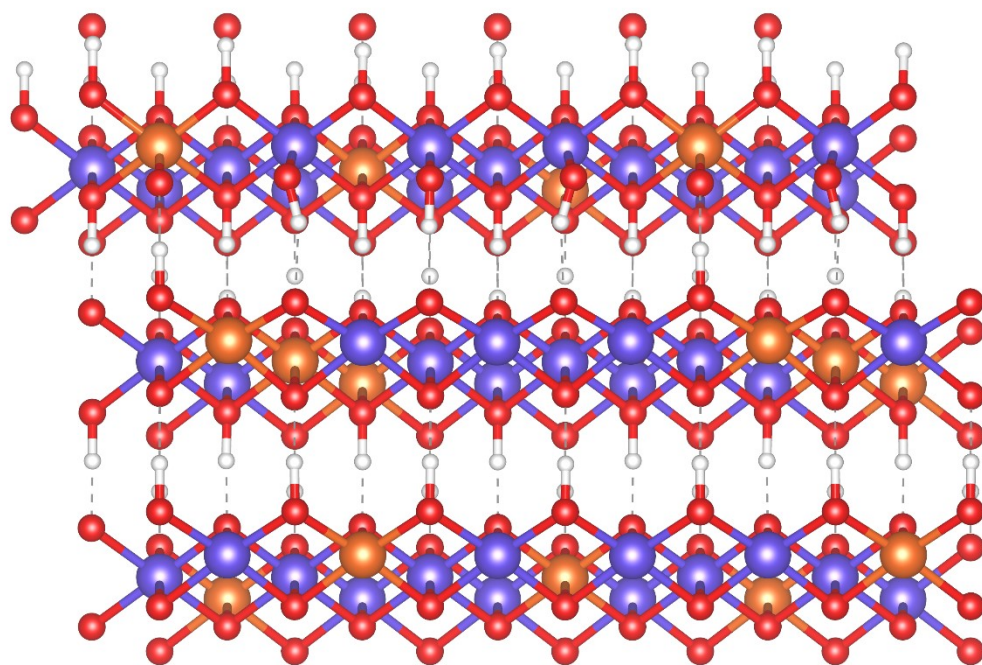
Fig. S29 Model structure of (a) $Fe_{0.25}Co_{0.75}OOH$.
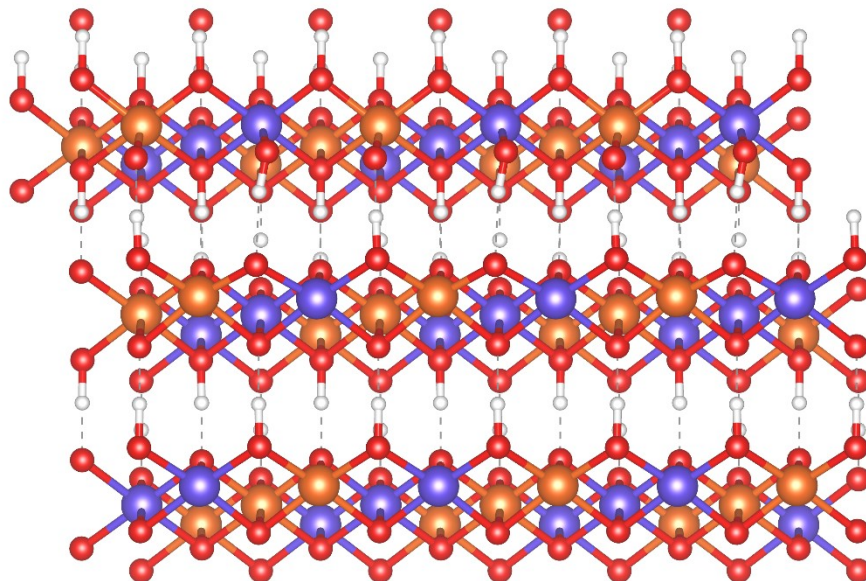
Fig. S30 Model structure of (a) $Fe_{0.50}Co_{0.50}OOH$.
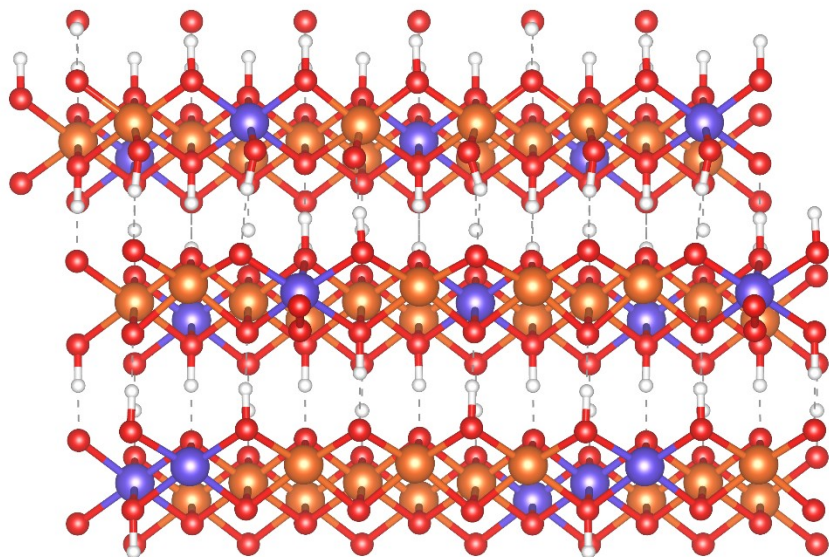
Fig. S31 Model structure of (a) $Fe_{0.75}Co_{0.25}OOH$.
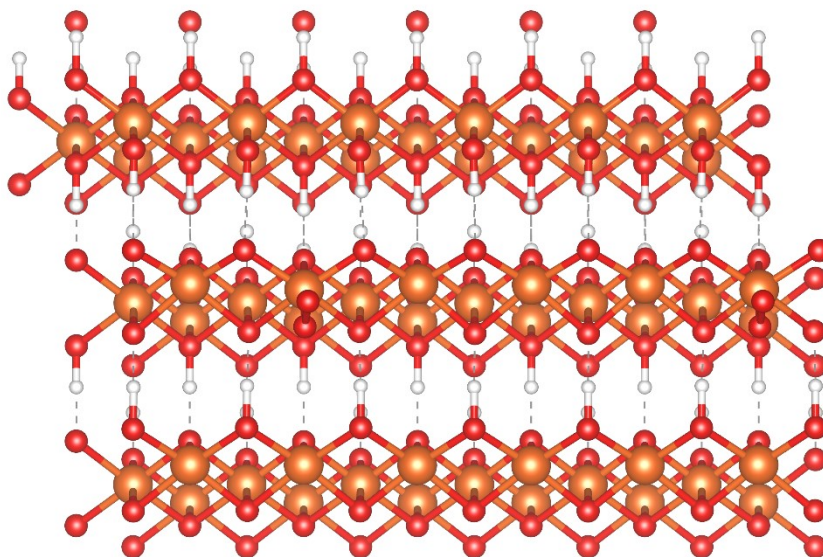
Fig. S32 Model structure of (a) FeOOH.
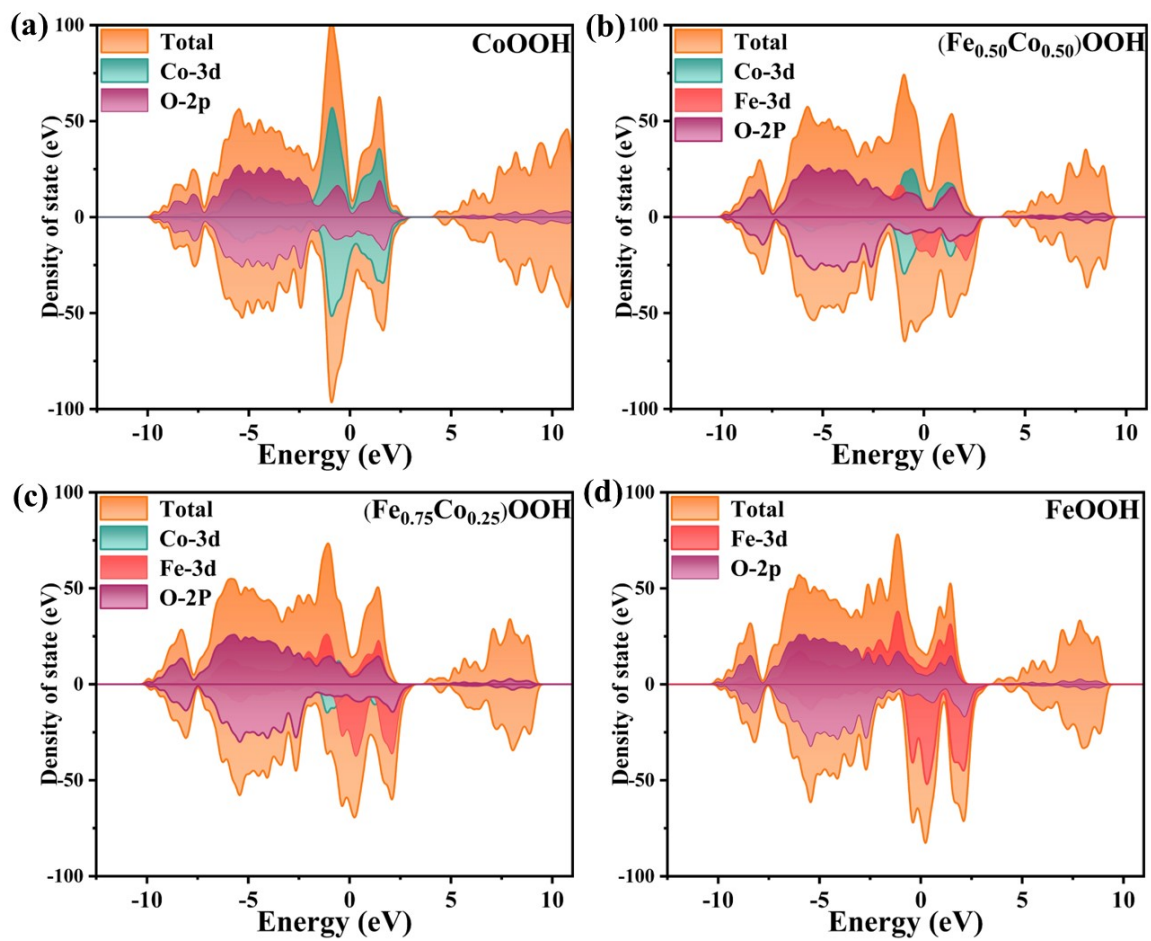
Fig. S33 The DOS of (a) CoOOH, (b) Fe$_{0.50}$Co$_{0.50}$OOH, (c) Fe$_{0.75}$Co$_{0.25}$OOH and (d) FeOOH..
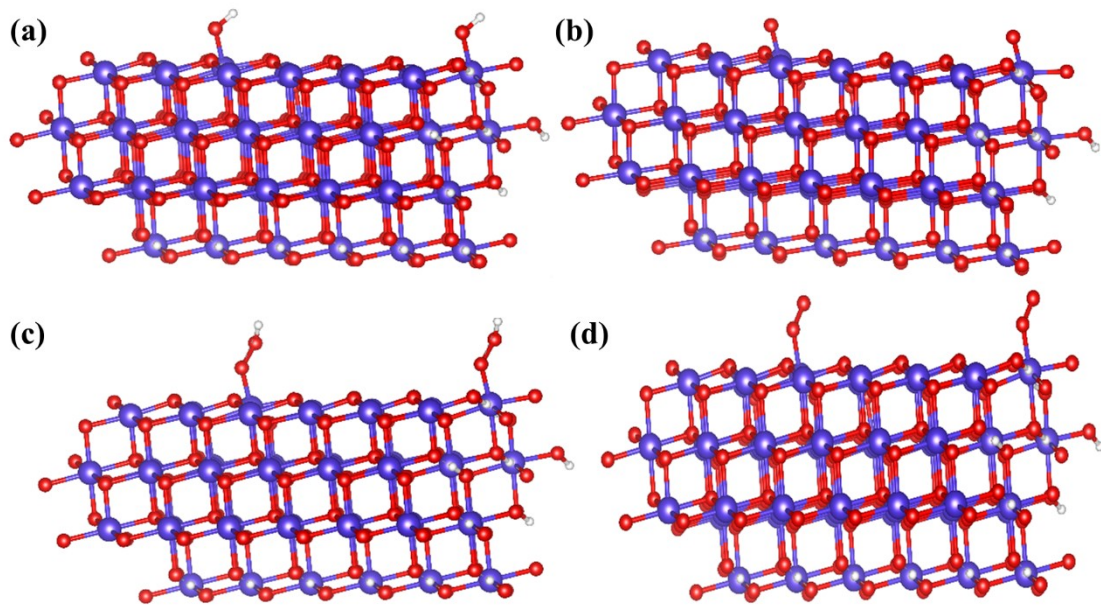
Fig. S34 The adsorption configuration of oxygen-containing intermediates on CoOOH.
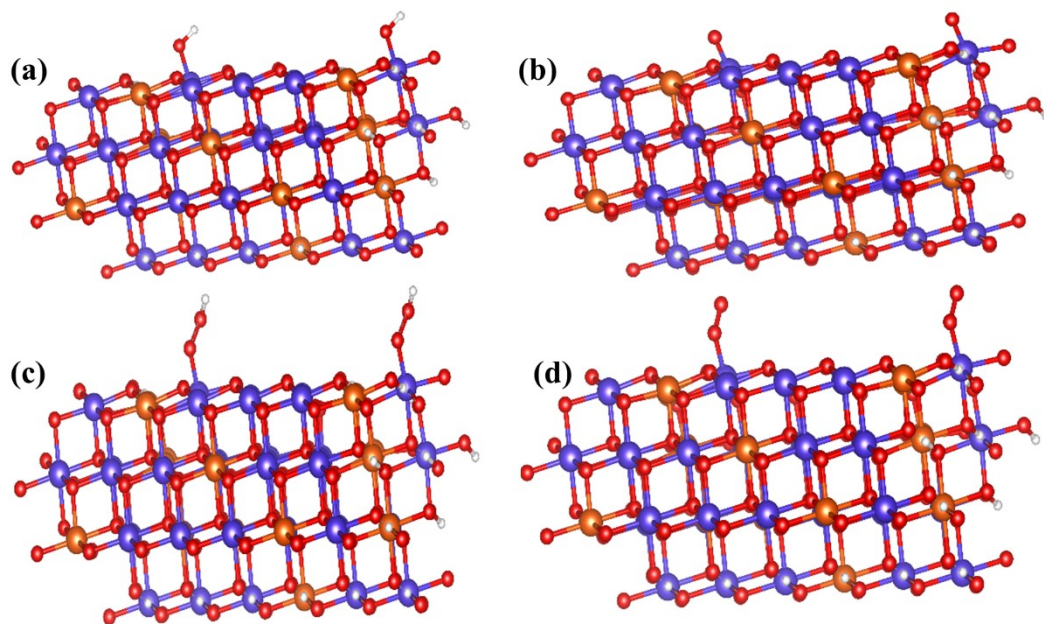
Fig. S35 The adsorption configuration of oxygen-containing intermediates on $Fe_{0.25}Co_{0.75}OOH$.
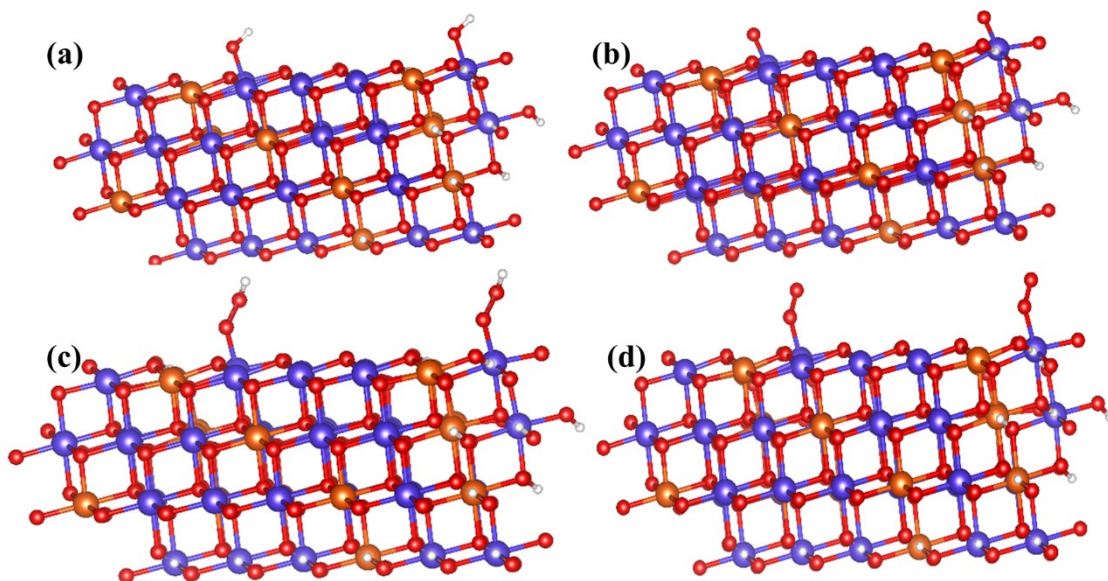
Fig. S36 The adsorption configuration of oxygen-containing intermediates on $Fe_{0.50}Co_{0.50}OOH$.
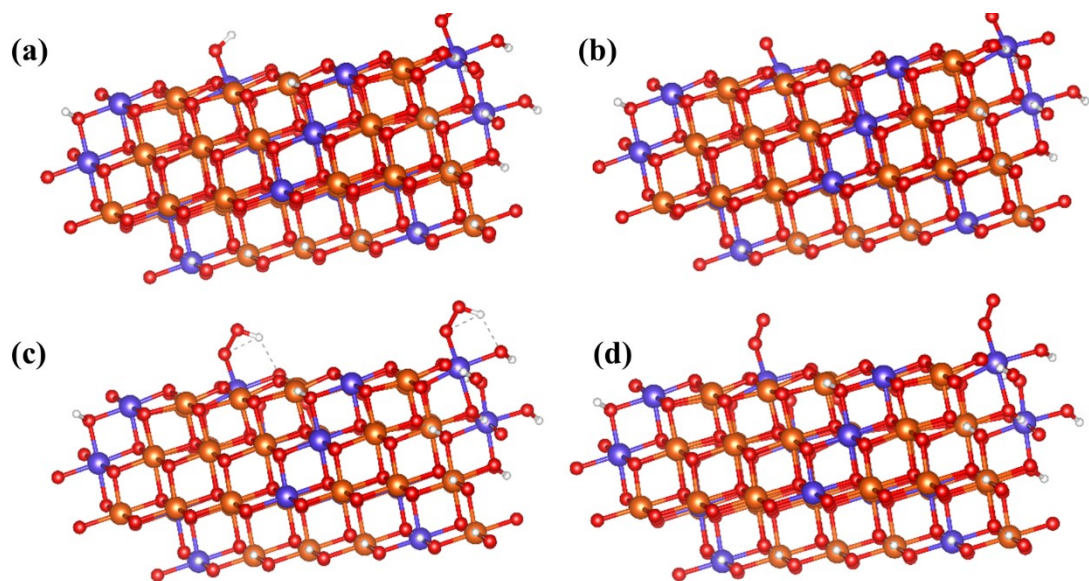
Fig. S37 The adsorption configuration of oxygen-containing intermediates on $Fe_{0.75}Co_{0.25}OOH$.
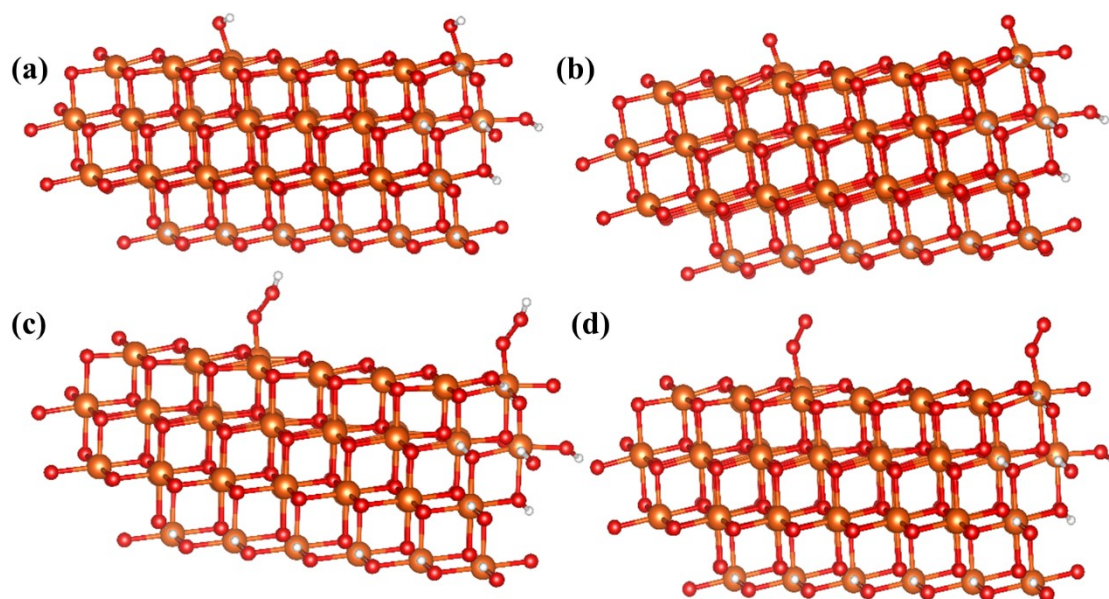
Fig. S38 The adsorption configuration of oxygen-containing intermediates on FeOOH.

Table S1. atomic content of $(Fe_xCo_{1-x})S_2$ samples by SEM-EDS.

Samples	Co (At%)	Fe (At%)	S (At%)
CoS_2	32	/	68
$(Fe_{0.16}Co_{0.84})S_2$	27.5	5.3	67.2
$(Fe_{0.20}Co_{0.80})S_2$	26.9	6.1	67.0
$(Fe_{0.25}Co_{0.75})S_2$	25.2	9.0	65.8
$(Fe_{0.33}Co_{0.67})S_2$	21.5	10.6	67.9
$(Fe_{0.50}Co_{0.50})S_2$	16.8	15.9	67.3
FeS_2	/	33.0	67.0

Table S2 XPS spectra of different catalysts with Co 2p.

Samples	$Co^{2+}2p_{1/2}$	$Co^{3+}2p_{1/2}$	$Co^{2+}2p_{1/2}$	$Co^{3+}2p_{1/2}$
CoS_2	780.77	783.20	797.08	800.51
$(Fe_{0.33}Co_{0.67})S_2$	781.83	783.90	798.43	802.44
$(Fe_{0.25}Co_{0.75})S_2$	781.69	783.79	798.21	802.06
$(Fe_{0.20}Co_{0.80})S_2$	781.46	783.27	798.05	800.57

Table S3 Component ratio (at %) of Co^{3+}/Co^{2+} in sample $(Fe_xCo_{1-x})S_2$ catalysts by XPS.

Samples	Co^{3+}/Co^{2+}
CoS_2	1.53
$(Fe_{0.33}Co_{0.67})S_2$	1.57
$(Fe_{0.25}Co_{0.75})S_2$	1.66
$(Fe_{0.20}Co_{0.80})S_2$	1.70

Table S4 XPS spectra of different catalysts with Fe 2p.

Samples	$Fe^{2+}2p_{1/2}$	$Fe^{3+}2p_{1/2}$	$Fe^{2+}2p_{1/2}$	$Fe^{3+}2p_{1/2}$	Fe-N_x $2p_{1/2}$	Fe-N_x $2p_{1/3}$
$(Fe_{0.33}Co_{0.67})S_2$	712.63	716.11	724.58	726.61	709.67	722.29
$(Fe_{0.25}Co_{0.75})S_2$	712.71	716.26	725.08	727.05	709.71	722.40
$(Fe_{0.20}Co_{0.80})S_2$	712.79	716.54	725.18	727.87	709.83	722.54

Table S5 Component ratio (at %) of N in sample $(Fe_xCo_{1-x})S_2$ catalysts by XPS.

Samples	Different N Components (at%)				
	Pyridinic-N	Fe-Nx	Pyrrolic-N	Graphitic-N	Oxidized-N
$(Fe_{0.33}Co_{0.67})S_2$	5.15%	8.80%	25.40%	42.87%	17.78%
$(Fe_{0.25}Co_{0.75})S_2$	7.05%	4.79%	37.55%	33.69%	16.92%
$(Fe_{0.20}Co_{0.80})S_2$	2.66%	4.44%	36.69%	39.51%	16.70%

Table S6 Comparison of OER activity of the reported electrocatalyst.

Ref	Catalyst	Overpotential at 10 mA cm^{-2} (mV)	Tafel slope (mV·dec^{-1})	Electrolyte
This work	$(Fe_{0.25}Co_{0.75})S_2$	274	29.6	1.0 M KOH
1	CoS_2	300	81	1.0 M KOH
2	CoS_2/Cu_2S-NF	348	92	1.0 M KOH
3	$Co_2O_4@CoS$/NF	290	1.61	1.0 M KOH
4	$Fc\text{-}Co_xS_y$	304	54.2	1.0 M KOH
5	meso-$FeMoS_2/CoMo_2S_4$	290	65	1.0 M KOH
6	Co_9S_8/N, P-APC	363	94.7	1.0 M KOH
7	$Co_9S_8@TDC$-900	330	86	1.0 M KOH
8	$Co_xNi_{1-x}S_2$ (CNS)/rGO	330	46	1.0 M KOH
9	$MoS_2/NiCoS$	290	77	1.0 M KOH
10	$Co_3S_4@MoS_2$	280	43	1.0 M KOH

Table S7 Summary the fitting parameters of the electrochemical impedance spectra.

Catalyst	R_s	R_{ct}
$(Co_{0.50}Fe_{0.50})S_2$	1.96	25.22
$(Co_{0.67}Fe_{0.33})S_2$	2.09	11.34
$(Co_{0.25}Fe_{0.75})S_2$	1.98	8.95
$(Co_{0.80}Fe_{0.20})S_2$	2.07	13.13
$(Co_{0.84}Fe_{0.16})S_2$	1.93	24.13
CoS_2	2.09	38.77
FeS_2	2.04	88.08

Table S8. Atomic content of $(Fe_{0.25}Co_{0.75})S_2$ after OER stability test by SEM-EDS.

Samples	Co (At%)	Fe (At%)	O (At%)
$(Fe_{0.25}Co_{0.75})OOH$	25.2	9.0	65.8

References

1   Y. Kang, Y. He, D. Pohl, B. Rellinghaus, D. Chen, M. Schmidt, V. Suss, Q. Mu, F. Li, Q. Yang, H. Chen, Y. Ma, G. Auffermann, G. Li and C. Felser, Identification of interface structure for a topological CoS_2 single crystal in oxygen evolution reaction with high intrinsic reactivity, *ACS Appl. Mater. Interfaces*, 2022, **14**, 19324-19331.

2   W. Li, L. Wu, X. Wu, C. Shi, Y. Li, L. Zhang, H. Mi, Q. Zhang, C. He and X. Ren, Regulation and mechanism study of the CoS_2/Cu_2S-NF heterojunction as highly-efficient bifunctional electrocatalyst for oxygen reactions, *Appl. Catal. B: Environ.*, 2022, **303**, 120849.

3   S. Adhikari, Y. Kwon and D.-H. Kim, Three-dimensional core–shell structured $NiCo_2O_4@CoS$/Ni-Foam electrocatalyst for oxygen evolution reaction and electrocatalytic oxidation of urea, *Chem. Eng. J.*, 2020, **402**, 126192.

4   P. Thangasamy, S. Oh, S. Nam, H. Randriamahazaka and I. K. Oh, Ferrocene-incorporated cobalt sulfide nanoarchitecture for superior oxygen evolution reaction, *Small*, 2020, **16**, 2001665.

5   Y. Guo, J. Tang, J. Henzie, B. Jiang, W. Xia, T. Chen, Y. Bando, Y.-M. Kang, M. S. A. Hossain, Y. Sugahara and Y. Yamauchi, Mesoporous Iron-doped MoS2/CoMo2S4 Heterostructures through Organic–Metal Cooperative Interactions on Spherical Micelles for Electrochemical Water Splitting, *ACS Nano*, 2020, **14**, 4141-4152.

6   X. Hu, Y. Chen, M. Zhang, G. Fu, D. Sun, J.-M. Lee and Y. Tang, Alveolate porous carbon aerogels supported Co_9S_8 derived from a novel hybrid hydrogel for bifunctional oxygen electrocatalysis, *Carbon*, 2019, **144**, 557-566.

7   J.-Y. Zhao, R. Wang, S. Wang, Y.-R. Lv, H. Xu and S.-Q. Zang, Metal–organic framework-derived Co_9S_8 embedded in N, O and S-tridoped carbon nanomaterials as an efficient oxygen bifunctional electrocatalyst, *J. Mater. Chem. A*, 2019, **7**, 7389-7395.

8   Y.-R. Hong, S. Mhin, K.-M. Kim, W.-S. Han, H. Choi, G. Ali, K. Y. Chung, H. J. Lee, S.-I. Moon, S. Dutta, S. Sun, Y.-G. Jung, T. Song and H. Han, Electrochemically activated cobalt nickel sulfide for an efficient oxygen evolution reaction: partial amorphization and phase control, *J. Mater. Chem. A*, 2019, **7**, 3592-3602.

9   C. Qin, A. Fan, X. Zhang, S. Wang, X. Yuan and X. Dai, Interface engineering: few-layer MoS_2 coupled to a NiCo-sulfide nanosheet heterostructure as a bifunctional electrocatalyst for overall water splitting, *J. Mater. Chem. A*, 2019, **7**, 27594-27602.

10   Y. Guo, J. Tang, Z. Wang, Y.-M. Kang, Y. Bando and Y. Yamauchi, Elaborately assembled core-shell structured metal sulfides as a bifunctional catalyst for highly efficient electrochemical overall water splitting, *Nano Energy*, 2018, **47**, 494-502.